

Interpreting Eruptive Behavior in NOAA AR 11158 via the Region's Magnetic Energy and Relative Helicity Budgets

Kostas Tziotziou & Manolis K. Georgoulis¹

*Research Center for Astronomy and Applied Mathematics (RCAAM)
Academy of Athens, 4 Soranou Efessiou Street, Athens, GR-11527, Greece*

and

Yang Liu

*W.W. Hansen Experimental Physics Laboratory, Stanford University,
Stanford, CA 94305-4085, USA*

ABSTRACT

In previous works we introduced a nonlinear force-free method that self-consistently calculates the instantaneous budgets of free magnetic energy and relative magnetic helicity in solar active regions (ARs). Calculation is expedient and practical, using only a single vector magnetogram per computation. We apply this method to a timeseries of 600 high-cadence vector magnetograms of the eruptive NOAA AR 11158 acquired by the Helioseismic and Magnetic Imager onboard the Solar Dynamics Observatory over a five-day observing interval. Besides testing our method extensively, we use it to interpret the dynamical evolution in the AR, including eruptions. We find that the AR builds large budgets of *both* free magnetic energy and relative magnetic helicity, sufficient to power many more eruptions than the ones it gave within the interval of interest. For each of these major eruptions, we find eruption-related decreases and subsequent free-energy and helicity budgets that are consistent with the observed eruption (flare and coronal-mass-ejection [CME]) sizes. In addition, we find that (1) evolution in the AR is consistent with the recently proposed (free) energy – (relative) helicity diagram of solar ARs, (2) eruption-related decreases occur *before* the flare and the projected CME-launch times, suggesting that CME progenitors precede flares, and (3) self-terms of free energy and relative helicity most likely originate from respective mutual-terms, following a progressive mutual-to-self conversion

¹Marie Curie Fellow.

pattern that most likely stems from magnetic reconnection. This results in the non-ideal formation of increasingly helical pre-eruption structures and instigates further research on the triggering of solar eruptions with magnetic helicity firmly placed in the eruption cadre.

Subject headings: Sun: activity Sun: coronal mass ejections Sun: evolution
Sun: flares Sun: magnetic fields Sun: photosphere

1. Introduction

A physically meaningful way to quantify the non-potentiality or, in other words, the eruptive capacity of solar active regions (ARs) is by calculating these regions’ non-potential, “free” magnetic energy and, perhaps, the associated (relative) magnetic helicity. The free magnetic energy is the excess energy stored in the magnetic configuration of ARs, above the reference, potential energy corresponding to the AR’s magnetic energy in the absence of electric currents. Magnetic helicity, on the other hand, is the corresponding degree of twist, writhe, and linkage of the AR’s magnetic field lines (Berger 1999, and references therein). Adopting the formalism of the *relative* magnetic helicity (Berger 1984), necessary in case the studied magnetic configuration permeates a given boundary (such as the photosphere, for ARs), nonzero (left- or right-handed) total magnetic helicity implies nonzero free energy. On the other hand, zero magnetic helicity, as a signed quantity, may imply a nonzero free magnetic energy, in case equal and opposite amounts of left- and right-handed helicity are simultaneously present in the configuration. Lack of electric currents automatically means a zero free magnetic energy and a zero relative helicity, at the same time meaning inability of an AR to energetically power solar eruptions, that is, flares and coronal mass ejections (CMEs) (e.g. Schrijver 2009, and references therein).

Contrary to free magnetic energy, a possibly decisive role of magnetic helicity in solar eruptions is strongly debated. While free magnetic energy dissipates in non-ideal processes such as magnetic reconnection, helicity is – to a very good approximation – conserved in the course of reconnection. Indeed, helicity dissipation appears proportional to the inverse square of the magnetic Reynolds number (e.g., Freedman & Berger 1993; Berger 1999), and this makes it insignificant for the solar atmosphere given the very large value of the latter. If not transferred due to reconnection via existing magnetic connections to larger scales, therefore (i.e. in remote parts of the global solar magnetic field), then helicity can be bodily removed from ARs in the form of CMEs (Low 1994; DeVore 2000). In smaller amounts, helicity can also escape to the heliosphere via unwinding motions of “open” magnetic field lines in case helical, “closed” field lines transfer their helicity to them via interchange reconnection (e.g.,

Pariat et al. 2009; Raouafi et al. 2010).

Outstanding questions that might well involve magnetic helicity and its evolution in the solar AR corona include (1) the triggering of solar eruptions and (2) the causal relationship between the two eruption aspects, namely flares and CMEs (a.k.a. the *flare-CME connection*). Numerous observational and modeling efforts have long suggested that ARs with large helicity budgets tend to be more eruptive than others (e.g., Canfield et al. 1999; Nindos & Andrews 2004; LaBonte et al. 2007; Nindos 2009; Georgoulis et al. 2009; Smyrli et al. 2010; Tziotziou et al. 2012) with some of these works actually attributing eruption onset to helicity, via the helical kink instability (e.g. Rust & LaBonte 2005; Török & Kliem 2005; Gibson et al. 2006; Kumar et al. 2012). A “large” helicity budget implies a *dominant* sign of helicity in ARs. On the other hand, there have been counterarguments over helicity’s necessity for eruptions in successful eruption models that utilize roughly equal and opposite amounts of left- and right-handed helicity (Phillips et al. 2005; Zuccarello et al. 2009).

A reasonable step ahead would be to simultaneously and self-consistently calculate the budgets of free magnetic energy and relative magnetic helicity in solar ARs. Existing, widely-applied techniques to this purpose involve time-integration of the relative-helicity and energy injection rates obtained via the Poynting theorem for helicity and energy, respectively, on the photospheric boundary (e.g., Berger & Field 1984; Kusano et al. 2002) or evaluation of the relative-helicity formula in the three-dimensional active-region corona (Berger 1984; Finn & Antonsen 1985). Both approaches have nontrivial prerequisites: helicity- and energy-rate calculation require a photospheric flow-velocity field that involves significant uncertainties (e.g., Welsch et al. 2007), together with the field-generating vector potential in the lower boundary (Chae 2001). Volume-calculation of helicity and energy, on the other hand, require an extrapolated three-dimensional magnetic field and its generating vector potential, including the corresponding current-free field and vector potential. Furthermore, nonlinear force-free (NLFF) field extrapolations are model-dependent and subject to uncertainties and ambiguities (Schrijver et al. 2006; Metcalf et al. 2008). Besides the computational expense stemming from the current spatial-resolution capabilities of observed solar vector magnetograms that render these calculations (particularly the volume calculation) infeasible for routine use, the additional prerequisites contribute to our overall inability to credibly monitor the magnetic energy and helicity budgets in solar ARs.

With these limitations in mind, Georgoulis & LaBonte (2007) introduced a technique that calculates the snapshot (instantaneous) free-magnetic-energy and relative-magnetic-helicity budgets in solar ARs using *only* a single vector magnetogram for each calculation. The calculation is self-consistent and strictly adopts the relative-helicity formulation (i.e., a zero relative helicity for a zero free energy). However, this first effort assumed linear

force-free fields that are known to be unrealistic for solar ARs. Recently, Georgoulis et al. (2012a) generalized the method to accommodate NLFF fields for the first time. Again, the method does not require any extrapolations, velocities, or vector-potential calculations. Tziotziou et al. (2012) applied this method to 162 vector magnetograms of 42 different ARs to construct the first free-magnetic-energy – relative-magnetic-helicity (EH) diagram of solar ARs. They reported a monotonic relation between free energy and relative helicity, thereby concluding that eruptive ARs tend to accumulate large budgets of *both* quantities. They further inferred well-defined thresholds of free energy and relative helicity for ARs to enter major (at least M-class) flaring and/or eruptive territory. These thresholds are 4×10^{31} erg and 2×10^{42} Mx², respectively. Calculation is straightforward and needs only a small fraction of the computational resources needed for a more conventional calculation of free energy and helicity budgets.

These developments occurred in excellent timing with the advent of the Solar Dynamics Observatory (SDO) mission (Pesnell et al. 2012) featuring the Helioseismic and Magnetic Imager (HMI) vector magnetograph (Scherrer et al. 2012). Besides the constant-quality, high-spatial-resolution SDO/HMI data, the instrument’s distinguishing feature is its unprecedented cadence. This has led to detailed, lengthy timeseries of AR vector magnetograms acquired within 12 minutes from each other. Such timeseries are ideal for the NLFF energy/helicity calculation method of Georgoulis et al. (2012a) in an effort to (a) test the method extensively, (b) investigate the statistical robustness of the EH diagram of Tziotziou et al. (2012), and (c) address the aforementioned outstanding questions regarding free-energy, helicity, and their combined or distinct role in solar eruptions.

From the so-far released SDO/HMI data sets, NOAA AR 11158 is undoubtedly the best-studied subject (see Section 3 below). The intensely eruptive AR gave the first X-class flare of solar cycle 24, thus ending the unusually prolonged lull of solar eruptive activity associated with the latest solar minimum. The SDO/HMI timeseries covered a 5-day interval of the evolution of the AR, including the major X2.2 flare and a lengthy series of other eruptive and combined flares.

This work is structured as follows: the SDO/HMI data on NOAA AR 11158 are described in Section 2. A brief overview of existing studies on the AR is presented in Section 3. Section 4 presents a summary of the methodology of Georgoulis et al. (2012a) for the calculation of free magnetic energy and relative magnetic helicity, as well as one of the most credible methods for deriving these budgets from time-integration of the respective injection rates. This latter method is used as reference for comparison with our instantaneous NLFF budget calculation. Section 5 provides our results in detail, while Section 6 summarizes the study, discusses the ramifications of our results, and presents our conclusions.

2. Data description

NOAA active region (AR) 11158 emerged in the eastern solar hemisphere, near disc center, on 2011 February 11. During its first disc transit, *GOES* 1-8 Å X-ray flux detectors registered 56 C-class, 5 M-class, and the first X-class (X2.2) flare of solar cycle 24 (01:44 UT on 2011 February 15) as stemming from this AR. The X-class flare was associated with conspicuous halo-CME and EUV wave events (Schrijver et al. 2011). The AR evolved quickly from a simple dipole to a complex, predominantly quadrupolar configuration with an enhanced and strongly sheared polarity inversion line (PIL). Snapshots of this rapid, dynamical evolution are presented in Figure 1. Extensive descriptions of the AR’s configuration and evolution can be found in Schrijver et al. (2011), Jiang et al. (2012), Liu et al. (2012b) and Vemareddy et al. (2012a), while Sun et al. (2012a) provided a detailed description of the long-term evolution of the AR, its magnetic field, and observed shear motions along the main PIL. A discussion of the most important works in the AR is presented in Section 3.

For our analysis we use cutout vector magnetic field data taken with the HMI onboard SDO. HMI is a full disk (4096×4096) filtergraph with a $0.5''$ pixel size that samples the Fe I 617.3 nm photospheric line through a 76 mÅ filter at six wavelength positions along the line, thus covering a range of $\lambda_0 \pm 17.5$ pm. The first of HMI’s two CCD cameras records filtergrams at these six wavelength positions in two polarization states and uses them to obtain Dopplergrams and line-of-sight (LOS) magnetograms at a cadence of 45 s. The second camera acquires six polarization states at these six wavelength positions every 135 s and uses them to compute the four Stokes parameters (I , Q , U , and V) necessary to derive the vector magnetic field. This is accomplished by a Milne-Eddington-based inversion approach (Borrero et al. 2011). Averaged 720-second filtergrams are used for the derivation of the Stokes parameters in order to enhance the signal-to-noise ratio and suppress 5-min p-mode oscillations.

We use 600 vector magnetograms of NOAA AR 11158 covering a five-day period (2011 February 12-16) with a 12-minute cadence. The photospheric area covered by these magnetograms is 650×600 pixels, or $325'' \times 300''$ on the image (observer’s) plane. Figure 1 provides a sequence of snapshots and a detailed vector magnetogram of the region. The vector magnetogram data were acquired by SDO’s Joint Science Operations Center (JSOC). Although the released vector magnetograms were already treated for the azimuthal 180° ambiguity, for reasons explained in Georgoulis (2012) they were re-processed using the non-potential field calculation (NPFC) of Georgoulis (2005), as revised in Metcalf et al. (2006). For our analysis we use the heliographic components of the magnetic field vector on the heliographic plane, derived with the de-projection equations of Gary & Hagyard (1990). As typical single-value uncertainties for the line-of-sight and transverse field components and for the azimuth angle

(δB_l , δB_{tr} and $\delta\phi$ respectively), we use the mean value of the JSOC-provided respective uncertainties of all pixels with a line-of-sight field B_l lying within 30% of the magnetogram’s maximum/minimum B_l value. This guarantees the exclusion of numerous quiet-Sun pixels within the field of view, with B_l values close to the derived errors, that would contribute with unrealistically high for an AR magnetic-field and azimuth-angle uncertainties. The mean values of the derived errors are $\delta B_l \sim 32.5$ G, $\delta B_{tr} \sim 38.2$ G and $\delta\phi \sim 2.9^\circ$.

Figure 2 shows the evolution of the unsigned (total) magnetic flux (thick black curve) and the corresponding positive- and negative-polarity fluxes (red and blue curves, respectively) over the observing interval. The thick orange curve denotes the unsigned magnetic flux participating in the magnetic connectivity matrix of the AR (see Section 4.1 for a definition) which is necessary for our calculations. Notice that the AR was approximately flux-balanced, with the positive-polarity flux showing a small ($\sim 5\%$ on average) excess over its negative-polarity counterpart. The dynamical evolution of the AR kicks in after decimal day 12.8 ($\sim 19:00$ UT on 2011 February 12) and is signaled by the abrupt increase of all flux budgets, particularly the unsigned connected flux (orange curve). Subsequent increases and decreases of this flux budget reflect the physical evolution in the AR, from flux emergence and enhancement of the connectivity matrix to flaring and eruptions (see Section 5.3 for a detailed description). During the observing interval the AR released one X-class, 3 M-class and 25 C-class flares.

3. NOAA AR 11158 in literature

NOAA AR 11158 has already been the subject of numerous studies, using a variety of methods and observations, and also including the same HMI data set used for the present study. Schrijver et al. (2011) presented the first detailed work, supported by MHD modeling, on several aspects of the X2.2 flare of February 15, 2011 such as the study of expanding loops above the PIL, the observed EIT wave event and the accompanying halo CME. The evolution of magnetic field and magnetic energy in NOAA AR 11158 were discussed in detail by Sun et al. (2012a) with the use of NLFF field extrapolations. More recently, Sun et al. (2012b) focused on the M2.2 flare triggered on February 14, 2011 and used NLFF field extrapolations to study non-radial eruptions modulated by the local magnetic field geometry and the existence of a coronal null point.

Several studies focused on horizontal fields, shear motions along the PIL, Lorentz-force calculations, and peculiar flows (proper motions) in NOAA AR 11158. A NLFF field-computation of the M6.6 flare of February 13 (Liu et al. 2012b) showed an 28%-increase of the mean horizontal field near the magnetic polarity inversion line (PIL) and a downward

collapse of a strong horizontal current system above the AR’s photosphere after the flare. Wang et al. (2012) reported a similar result for the X2.2 flare, showing a rapid, irreversible enhancement (30%) of the horizontal magnetic field at the PIL and an increase of both inclination and shear of the photospheric field as a response to the flare. This agrees with the results of Sun et al. (2012a) who used a NLFF field extrapolation to show an enhancement of the horizontal field that becomes both more inclined and more parallel to the PIL. Gosain (2012) also found that the field became more horizontal after the flare close to the PIL. Jiang et al. (2012) detected a clockwise rotation in the sunspot, 20 hours prior to the X-class flare that stopped one hour after the flare and suggested that these motions were associated with the buildup of helicity in the region and the shearing of the main neutral line. Abrupt changes during the X2.2 flare in the vertical electric current, the Lorentz force vector and the field vector, that became stronger and more horizontal, were also described by Petrie (2012); these changes were mainly concentrated near the PIL where the shear increased. Alvarado-Gómez et al. (2012) used HMI dopplergram data to identify, through standard methods of local helioseismology, seismic sources in the X2.2 flare event. They correlated these sources with the HMI magnetic-field changes and estimated the work done by the Lorentz force integrated over the entire AR. Liu et al. (2012a) studied photospheric flows derived from HMI vector fields and sub-photospheric flows derived by time-distance helioseismology from HMI dopplergrams to conclude that horizontal flows associated with flux emergence, including apparent shear motion along the PIL, do not extend deeply into the subsurface. Horizontal proper motions of a few 100 m s^{-1} along the main neutral line of the X2.2 flare were measured by Beauregard et al. (2012) using a local correlation tracking method on HMI continuum images and longitudinal magnetograms. Maurya et al. (2012) further reported magnetic and Doppler transients and locations of spectral line reversals during the flare’s impulsive phase that do not correspond to real changes of the photospheric magnetic and velocity field.

Concerning helicity budgets in NOAA AR 11158, Vemareddy et al. (2012a) studied the helicity injection (through shuffling) and its behavior and found that changes of the helicity flux signal due to injection of negative helicity in regions of dominant positive helicity are co-spatial and co-temporal with flaring/eruptive sites. Jing et al. (2012), using the same HMI vector magnetogram data set as our study, calculated the average current helicity as a function of altitude and relative helicity with a NLFF coronal field extrapolation method. Nindos et al. (2012), in a study of the role of the overlying background field in solar eruptions, also calculated from the same HMI vector magnetogram data the helicity flux and budget in NOAA AR 11158. Electric current, fractional current helicity (i.e., helicity due to vertical electric currents), photospheric free energy, and angular shear were also recently derived by Song et al. (2012) in an attempt to quantify the non-potentiality of NOAA AR 11158.

Vemareddy et al. (2012b), on the other hand, studied two sub-regions of the AR with rotating sunspots and showed that proper and rotational motions play a key role in enhancing the magnetic non-potentiality of the AR by injecting helicity and twisting the magnetic fields, thus increasing the free energy.

Recently, Liu & Schuck (2012), in a comprehensive study of magnetic helicity and energy in NOAA AR 11158, studied the region’s evolution by deriving and integrating helicity injection from both shuffling and emergence. They concluded that helicity is mainly contributed by shuffling while the energy build-up is mainly attributed to emergence.

Finally, a study of loops in NOAA AR 11158 was carried out by Aschwanden et al. (2011), who applied an automated analysis of SDO/AIA image datasets, to detect 570 loop segments, shortly before the X-class flare, at temperatures covering the range of $10^{5.7} - 10^7$ K. Gosain (2012) used SDO/AIA observations to also study the evolution of coronal loops during the X2.2 flare which show three distinct dynamical phases; a slow rise phase prior to the flare, a collapse phase during the flare and an oscillation phase following the flare-driven implosion.

4. Methodology: free magnetic energy and relative magnetic helicity budgets

In this Section we present a) our method for calculating the instantaneous free magnetic energy and relative magnetic helicity budgets in an AR (Section 4.1), and b) the derivation of these budgets by integrating the respective energy/helicity fluxes inferred via the photospheric velocity field (Section 4.2). We emphasize that the main analysis method is the one described in Section 4.1; integrated helicity and energy fluxes are used as a reference for comparison with our results.

4.1. NLFF energy and helicity budgets from single vector magnetograms

Recently, Georgoulis et al. (2012a) proposed a new NLFF method to derive the (instantaneous) free magnetic-energy and relative magnetic-helicity budgets using a single photospheric or chromospheric vector magnetogram of the studied AR. This method provides unique results, contrary to model-dependent NLFF field extrapolation methods. In return, it requires a unique magnetic-connectivity matrix, i.e., a matrix containing the flux committed to connections between positive- and negative-polarity flux partitions. This matrix is calculated using a simulated annealing method (Georgoulis & Rust 2007; Georgoulis et al. 2012a) that guarantees connections between opposite-polarity flux partitions while globally mini-

mizing the corresponding connection lengths. The connectivity matrix defines a collection of N magnetic connections, treated as slender force-free flux tubes with known footpoints, flux contents, and variable force-free parameters.

For this collection of flux tubes, the free magnetic energy E_c is the sum of a self term $E_{c_{\text{self}}}$, expressing the internal twist and writhe of each tube, and a mutual term $E_{c_{\text{mut}}}$, due to interactions between different flux tubes. As such, it is given by

$$\begin{aligned} E_c &= E_{c_{\text{self}}} + E_{c_{\text{mut}}} \\ &= Ad^2 \sum_{l=1}^N \alpha_l^2 \Phi_l^{2\delta} + \frac{1}{8\pi} \sum_{l=1}^N \sum_{m=1, l \neq m}^N \alpha_l \mathcal{L}_{lm}^{\text{arch}} \Phi_l \Phi_m, \end{aligned} \quad (1)$$

where A and δ are known fitting constants, d is the pixel size of the magnetogram and Φ_l and α_l are the respective flux and force-free parameters of flux tube l . $\mathcal{L}_{lm}^{\text{arch}}$ is the mutual-helicity factor of two arch-like flux tubes that do not wind around each other's axes. Inference of this factor, first introduced by Démoulin et al. (2006), is discussed in detail by Georgoulis et al. (2012a) for all possible cases of intersecting/non-intersecting flux tubes pairs and flux-tube pairs with a “matching” footpoint, per the reduced spatial resolution of the flux-partitioning map. Notice that the free energy of Equation (1) is to be taken as a *lower limit* of the actual energy as the unknown winding factor around flux tubes, that would require knowledge of the three-dimensional magnetic field, has been set to zero. Previous works (Georgoulis et al. 2012a; Tziotziou et al. 2012) have shown that this lower limit is realistic.

Likewise, the respective relative magnetic helicity H_m is the sum of a self $H_{m_{\text{self}}}$ and a mutual $H_{m_{\text{mut}}}$ term,

$$\begin{aligned} H_m &= H_{m_{\text{self}}} + H_{m_{\text{mut}}} \\ &= 8\pi d^2 A \sum_{l=1}^N \alpha_l \Phi_l^{2\delta} + \sum_{l=1}^N \sum_{m=1, l \neq m}^N \mathcal{L}_{lm}^{\text{arch}} \Phi_l \Phi_m. \end{aligned} \quad (2)$$

We refer the reader to Georgoulis et al. (2012a) for a detailed description of the method and the derivation of uncertainties for all terms of Equations (1) and (2).

4.2. NLFF energy and helicity budgets by integration of respective fluxes

A method to infer the (total) energy and relative helicity budgets in an active region at time t is by integrating the respective fluxes from initiation t_0 of the active region to time t . The energy and helicity budgets in this case are given by

$$E \equiv E(t) = \int_{t_0}^t (dE/dt) dt \quad (3)$$

and

$$H_m \equiv H_m(t) = \int_{t_0}^t (dH_m/dt)dt, \quad (4)$$

respectively, where $E(t_0) = H_m(t_0) = 0$. The helicity injection rate (Berger & Field 1984) depends on a) the photospheric velocity vector, whose inference involves significant uncertainties (e.g., Welsch et al. 2007), and b) the vector potential \mathbf{A}_p of the potential magnetic field \mathbf{B}_p exhibiting the same normal-field condition as the observed field \mathbf{B} .

In the simplest case, photospheric velocities can be inferred from a sequence of magnetograms through local correlation tracking (LCT; November & Simon 1988) techniques which, however, are highly uncertain due to the ambiguities in image motion. Moreover, LCT techniques tend to underestimate the amount of helicity injected by the shear term (Démoulin & Berger 2003) and are inconsistent with the magnetic induction equation, which governs the evolution of the photospheric magnetic fields (Schuck 2005).

Several alternative methods have been proposed during the past decade (see Welsch et al. 2007, and references therein) for the evaluation of plasma velocities. Here we use the Differential Affine Velocity Estimator for Vector Magnetograms (DAVE4VM) introduced by Schuck (2008), which is a generalization of the Differential Affine Velocity Estimator (DAVE; Schuck 2005, 2006) method. DAVE4VM estimates the plasma velocity \mathbf{v} using the normal component of the ideal induction equation

$$\partial_t B_z + \nabla_h \cdot (B_z \mathbf{v}_h - v_z \mathbf{B}_h) = 0, \quad (5)$$

where \mathbf{B} is the magnetic field vector, z denotes the normal (vertical) axis and h denotes x - and y -components on the tangential (horizontal) plane. We apply this method to our timeseries of vector magnetograms on the heliographic plane, using a window size of 21 pixels in DAVE4VM. Since the coordinate system for the affine velocity profile is not aligned with the magnetic field (velocities not necessarily orthogonal to \mathbf{B}), the calculated velocity \mathbf{v} has to be further corrected by removing the field-aligned plasma flow \mathbf{v}_{\parallel} and keeping only the perpendicular (\perp) component that plays a role in the induction equation. The corrected cross-field velocity is given by

$$\mathbf{v}_{\perp} = \mathbf{v} - \frac{(\mathbf{v} \cdot \mathbf{B})\mathbf{B}}{B^2}. \quad (6)$$

The normal $v_{\perp n}$ and tangential $v_{\perp t}$ components of this velocity \mathbf{v}_{\perp} are then used to calculate the helicity flux $\left. \frac{dH}{dt} \right|_S$ across the plane S of the magnetogram. As Berger & Field (1984) have shown, this is derived by

$$\left. \frac{dH}{dt} \right|_S = 2 \int_S (\mathbf{A}_p \cdot \mathbf{B}_h) v_{\perp n} dS - 2 \int_S (\mathbf{A}_p \cdot \mathbf{v}_{\perp t}) B_z dS, \quad (7)$$

where the first term roughly corresponds to the helicity flux through emergence and the second term to helicity flux through photospheric shuffling. The vector potential \mathbf{A}_p is calculated by means of a fast Fourier transform method, as implemented by Chae (2001). We refer the reader to Liu & Schuck (2012) for a discussion concerning issues related to the computation and interpretation of helicity fluxes related to tangential and vertical flows.

Likewise, the magnetic-energy injection rate (i.e., the Poynting flux) $\left. \frac{dE}{dt} \right|_S$, as Kusano et al. (2002) have shown, is given by

$$\left. \frac{dE}{dt} \right|_S = \frac{1}{4\pi} \int_S B_h^2 v_{\perp n} dS - \frac{1}{4\pi} \int_S (\mathbf{B}_h \cdot \mathbf{v}_{\perp t}) B_z dS \quad , \quad (8)$$

where the first term roughly corresponds to the energy flux through emergence and the second term to energy flux through shuffling.

5. Results

5.1. Helicity and energy budgets in NOAA AR 11158

We first apply the method described in Section 4.1 to the 600 SDO/HMI magnetograms of our sample. Figures 3 and 4 show respectively the relative magnetic helicity and the free magnetic energy budgets in the AR as functions of time. Totals (panels [b]) and self-terms (panels [c]) are also shown. Given the small amplitudes of the self terms for energy and helicity, the corresponding mutual terms are indistinguishable from the totals and are hence not shown here. Figure 4 also shows the potential and total magnetic energy and their evolution. Uncertainties are shown by grey bars in all plots. For the total and mutual energy/helicity terms these uncertainties are relatively small, while they are relatively large for the self terms.

All relative-helicity and free-energy terms show a relatively smooth, progressive evolution, with some scatter around the corresponding 72-min-running averages. Scatter increases after decimal day 13.5 when the AR starts building significant budgets of magnetic helicity and free energy powered by continuous flux emergence (Figure 2). An important finding is that the region builds *both* significant relative magnetic helicity and free magnetic energy, reaching peaks of $\sim 2 \times 10^{43} \text{ Mx}^2$ and $\sim 5.5 \times 10^{32} \text{ erg}$ respectively. These budgets are large enough to power several eruptive flares which, in fact, is what the AR did over the 5-day observation interval (Section 2). The peak times of all these flares are marked in Figures 3, 4. Eruptive flares can be assessed fairly easily by using frequency-time radio spectra such as those of Figures 3a, 4a, obtained by the WAVES instrument onboard the Wind mission

(Bougeret et al. 1995). Type-II radio activity in particular, corresponding to hours-long frequency drift of the radio emission, is a tell-tale signature of shock-fronted CMEs (see, e.g., Hillan et al. 2012, and references therein). Much faster (shorter) frequency drifts (Type-III bursts) typify magnetic-reconnection episodes in the solar atmosphere. Association of registered GOES flares with observed CMEs is based on a) correspondence of the peak time of the flare with the onset time of the Type-II radio burst, and b) available CME catalogues, such as the LASCO, CACTUS and SEEDS. This is because neither *GOES* nor *Wind*/WAVES have spatial resolution. While the flare-CME connection is discussed in Section 5.6 in more detail, from Figures 3a, 4a we discern that at least the M6.6 flare of February 13, the M2.2 flare of February 14, the X2.2 flare of February 15, and the M1.6 flare of February 16 were eruptive.

NOAA AR 11158, an intensely flaring/eruptive AR shows both a significant budget and a dominant sense of magnetic helicity, positive (right-handed) in this case, as already suggested by Tziotziou et al. (2012) for numerous ARs. Notably, as well, no major flare (\geq M1.0) occurs before thresholds of $\sim 4 \times 10^{31}$ erg and $\sim 2 \times 10^{42}$ Mx² in free magnetic energy and relative magnetic helicity, respectively, are exceeded, as concluded by Tziotziou et al. (2012). This point is further discussed in Section 5.4.

Comparison of our results (Figure 4) with the respective results by Sun et al. (2012a) shows that although the corresponding potential, total and free energy evolution share some qualitative resemblance before the occurrence of the X-class flare, there are notable differences in their evolution afterwards: the magnetic energy derived by Sun et al. (2012a) continuously decreases after the flare while in our case free energy increases for almost a day thereafter. Furthermore, there are quantitative differences within the entire observing interval with the maximum free magnetic energy derived by our NLFF method being almost twice that derived by the NLFF field extrapolation (notice that our free energy is a lower limit!). Similar differences also exist between our magnetic free energy and the respective results by Nindos et al. (2012), derived from NLFF field extrapolations of 16 *Hinode* SOT/SP vector magnetograms, that do not differ substantially from the results by Sun et al. (2012a). Such discrepancies are already noted and discussed by Georgoulis et al. (2012a). Finally, the relative helicity evolution derived by Jing et al. (2012) using a NLFF field extrapolation differs from our result both quantitatively and qualitatively, as it is $\sim 50\%$ lower.

5.2. Comparison with helicity/energy budgets derived from integration of helicity/energy fluxes

Figure 5 shows the emergence and shuffling terms of helicity (Figure 5a) and energy (Figure 5b) fluxes, as well as the their totals, derived by Equations (3) and (4). Emergence and shuffling terms of energy/helicity are always in phase, while changes in the evolution of both beyond the influence of flux emergence mainly reflect shear motions along the PIL, separation motions of connected polarities, and sunspot rotation (Liu & Schuck 2012). Shuffling dominates over emergence in helicity injection rates, while emergence dominates over shuffling in energy injection rates. Moreover, significant changes in the energy flux seem to occur immediately after the X-class flare (early on day 15) while there seems to be a ~ 24 -hour delay in the helicity flux response. As discussed in Section 4.2, magnetic-energy and helicity budgets at a given time are derived here by integrating the respective fluxes from the start of observation to the time of interest. These budgets should be good approximations of the actual budgets because the start of the observing interval corresponds practically to the birth (t_0) of the AR.

Integrating the helicity injection rates (Figure 5a) we find a total accumulated helicity $\sim 2.4 \times 10^{43} \text{ Mx}^2$, with almost two thirds of it due to shuffling. This is in agreement with the results of Liu & Schuck (2012). In terms of energy, we find a total accumulated value $\sim 9 \times 10^{32} \text{ erg}$, with $\sim 77\%$ of it due to emergence; this is slightly different than the percentages reported by Liu & Schuck (2012). We also note that both the shuffling helicity flux profile and the corresponding accumulated helicity are in fairly good agreement with the corresponding calculations of Vemareddy et al. (2012a) who used DAVE instead of DAVE4VM to derive the velocity flow field in the AR. However, Nindos et al. (2012), who also used DAVE for deriving the helicity flux, find an accumulated helicity which is almost 50% lower than our accumulated helicity due to shuffling.

The helicity and energy flux curves derived by Liu & Schuck (2012) show a qualitative agreement but significant quantitative differences with our helicity/energy-flux results. Differences stem mostly from a difference in the field-of-view (FOV) since these authors used a significantly smaller FOV that tightly encloses the AR. This difference in the FOV also explains the difference between our unsigned flux (Figure 2) and the corresponding flux derived by Liu & Schuck (2012) and Sun et al. (2012a) who used the same (albeit Lambert de-projected) magnetograms. Use of a ~ 200 -300 G threshold in our flux derivation, which is equivalent to restricting the FOV very close to the AR, results in a curve that is identical to theirs (not shown here). Further small discrepancies in the helicity flux could result from a) uncertainties in the velocity calculations, b) differences in the azimuth disambiguation methods, and c) differences in the de-projection of the magnetograms; as already mentioned,

Liu & Schuck (2012) used the Lambert (cylindrical equal area) de-projection method while we use the heliographic de-projection (Gary & Hagyard 1990).

Comparing the flux-integrated energy and helicity budgets from Section 4.2 with our respective NLFF budgets from Section 4.1 we find a fairly close agreement between the peaks, particularly for the relative helicity ($\sim 2 \times 10^{43} \text{ Mx}^2$ [instantaneous] vs. $\sim 2.4 \times 10^{43} \text{ Mx}^2$ [flux-integrated]) and less so for the total magnetic energy ($\sim 16 \times 10^{32} \text{ erg}$ [instantaneous] vs. $\sim 9 \times 10^{32} \text{ erg}$ [flux-integrated]). Comparing the respective temporal profiles is not straightforward, however, and could even be misleading: in our *instantaneous* NLFF budgets, activity-related changes reflected on the connectivity matrix incur a direct impact on the budget values. Flux-integrated budgets, on the other hand, will not show an activity-related change unless the photospheric velocity field, primarily, is impacted by this change. This explains the smoothness of the flux-integrated budgets in Figure 5 that is contrasted to the numerous transient variations of the (72-minute averaged) instantaneous budgets. Nonetheless, a point-to-point comparison between the integrated helicity/energy fluxes and the respective NLFF budgets yields significant correlations, at least up to the end of February 15, just before our instantaneous budgets started decreasing. We find linear (Pearson) and rank-order (Spearman) coefficients of the other 0.73 and 0.79, respectively, for relative magnetic helicity, and 0.83 and 0.84, respectively, for total magnetic energy.

Concluding, we note in passing that helicity- and energy-flux calculations and associated budgets “inherit” the uncertainties of the inferred photospheric velocity field, including caveats or shortcomings in its calculation. We repeated the analysis of Section 4.2 using a classical LCT method applied to successive sub-sequences of five consecutive B_z -images. We found that the LCT-calculated emergence helicity budget is roughly an order of magnitude smaller than that obtained using DAVE4VM-inferred velocities (Figure 5a).

5.3. Helicity and energy evolution in NOAA AR 11158

5.3.1. Comparison of helicity/energy budgets with unsigned connected flux

As already discussed in Section 2 and elsewhere, NOAA AR 11158 exhibited a very rapid and dynamical evolution, with continuous flux emergence (Figures 1 and 2) and a rapidly evolving connected flux (Figure 2). Connected-flux changes reflect changes in the connectivity matrix that arise from flux emergence, flux cancellation in small-scale reconnection events and/or large-scale flaring/erupting activity. Figures 3 and 4 suggest a good agreement between the unsigned connected flux and the AR’s relative helicity/free magnetic energy budgets with significant linear and rank-order correlation coefficients, equal to 0.93

and 0.89 for helicity and 0.88 (both correlation coefficients) for free magnetic energy. It is, however, the potential energy that shows a remarkable correlation with the unsigned connected flux with both correlation coefficients ~ 0.99 . This suggests that the unsigned flux evolution correlates well with the global magnetic-field evolution in the AR while small increases/decreases indicate local and/or larger-scale changes in the non-potentiality of the magnetic field configuration resulting, at times, in significant changes in the relative helicity and/or free magnetic energy budget. Point taken, we will now further discuss the dynamical evolution of NOAA AR 11158 by examining the evolution of magnetic helicity and free magnetic energy in more detail.

5.3.2. *Helicity evolution in NOAA AR 11158*

Figure 3 shows the evolution of relative magnetic helicity in NOAA AR 11158. In the pre-eruption phase of the AR, particularly during the first day (February 12, 2011), the relative helicity budget is very low. It reflects the initially simple β -configuration (Figure 1) of the AR, with a magnetic-field configuration apparently close to a potential configuration. However, the AR evolved rapidly, within a couple of days, into a more complex $\beta\gamma\delta$ -configuration (Figure 1). Consequently, the helicity budget increased drastically within less than a day starting around the end of February 12, a period that coincides with the first cluster of two C-class flares and an eruptive M6.6 flare (see Figures 3, 4 and 11). Several hours after the M-class flare, late on day 13, a significant decrease of helicity occurs, co-temporally with a small increase of the connected flux, which is not associated with any flaring/eruptive activity. This helicity decrease seems also to be associated with a delayed by 2 hours increase of the free magnetic energy (Figure 4) and probably suggests a large-scale re-organization of the AR. Thereafter, during the early hours of day 14, coinciding with a second cluster of four non-eruptive C-class flares (among them a C8.3 and a C6.6), helicity increases, but this is followed by a very significant, simultaneous decrease of helicity, free energy and connected magnetic flux shortly before midday (~ 14.4). Figure 6 indicates an intense restructuring of the magnetic-field configuration accompanied by an increase of the fragmentation in the AR. The former is reflected on the decrease of the connected flux Φ_{conn} while the latter is judged by the abrupt increase of the flux-tube number. “Open” flux is further increased, implying that previously connected flux within the AR now closes beyond the AR’s limits.

Helicity increases again, during the last half of day 14, when a swarm of six C-class flares (the largest ones being C9.4, C7 and an eruptive C6.6 [Figure 11]) and an eruptive M2.2 flare occur. An overall increasing helicity trend, starting around decimal day 14.5, interrupted by short, simultaneous decreases of helicity, free energy and connected flux associated with

eruptions (see further discussion in Section 11), could well be related to the reported rotation of the main sunspots (Jiang et al. 2012; Vemareddy et al. 2012a). Such a rotation twists and/or shears nearby magnetic field lines, adding further helicity and free/total energy to the region. Recently, Vemareddy et al. (2012b) showed clear correspondence, in a sub-region of NOAA AR 11158, between the rotational profile of the sunspot and the respective shear and helicity flux. This latest cluster of flares is followed in the early hours of day 15 by the large eruptive X2.2 flare, the first X-class flare of solar cycle 24. The peak of the helicity budget ($\sim 2 \times 10^{43} \text{ Mx}^2$) is first reached three hours after the X-class flare. The persistence of sunspot rotation after the X-class flare (Jiang et al. 2012) could explain this further increase of helicity.

It is worth-discussing further that during the aforementioned 1.5-day interval before the first helicity peak, despite the occurrence of eruptive flares that removed helicity from the AR, helicity kept on increasing. This behavior seems to be the end result of a continuous, uneven competition between new helicity injection in the region, as Figure 5 also suggests, and helicity removal through repetitive eruptive activity with the former overpowering the latter. There are, as expected, occasional decreases of helicity during this interval associated with eruptive flares, which will be later discussed in Section 5.6, but the magnetograms (Figure 1) attest to a very rapid and intense dynamical evolution of the AR, with continuous emergence of new magnetic flux. As a result, both the unsigned flux and the unsigned connected flux keep increasing throughout the interval of study (Figure 2). The latter generally follows the aforementioned helicity evolution, increasing rapidly between decimal days 12.7 to 15 and then fluctuating around a mean value of $2.4 \times 10^{22} \text{ Mx}$.

After its first peak, the helicity budget shows a considerable decrease that immediately follows the termination of the sunspot rotation reported by Jiang et al. (2012), and probably indicates another re-organization of the AR’s magnetic connectivity, after a large sequence of flaring/eruptive activity. This re-organization also relates to the decrease of the unsigned connected flux and the simultaneous increase of free magnetic energy. Figure 7, provides a glimpse of this re-organization with two connectivity matrices before and after the X-class flare, separated by an hour, that clearly show connectivity changes mainly between the AR’s eastern sunspot complex, where the flare occurred, and the AR’s central complex of sunspots. We also remind the reader that an EIT wave event (Schrijver et al. 2011) accompanied the X-class flare, which could affect the AR and its vicinity. Late on February 15, the helicity budget increases again through two non-eruptive C-class flares and reaches a second, similar peak at decimal day 15.84, at which time a C6.6 non-eruptive flare occurs. Thereafter, a substantial, 30% helicity decrease occurs within 8 hours, accompanied only by two small non-eruptive C-class flares. This remarkable helicity decrease also coincides with a considerable decrease of free magnetic energy and, as Figure 8 shows, a decrease of the connected flux. At

the same time the number of flux tubes that comprise the connectivity matrices increases, indicating a rapid fragmentation of the AR (more magnetic partitions, defining a larger number of flux tubes but with less total connected flux), while the open flux also increases indicating a large-scale re-organization of the magnetic configuration. It is the cumulative effect of both processes that leads to these observed helicity and energy decreases while no eruptive activity takes place.

During the last 17 hours of February 16, 2011 seven non-eruptive C-class flares (among them a C9.9 and a C7.7) and an eruptive M1.6 flare occur while the helicity fluctuates around a value of $\sim 1.5 \times 10^{43} \text{ Mx}^2$. This well-defined mean helicity, despite a swarm of (non-eruptive) flares, relates to the absence of major eruptions during this interval - only the eruptive M1.6 flare shows a clear associated helicity decrease (see Section 5.6 and Figure 11).

5.3.3. *Free magnetic energy evolution in NOAA AR 11158*

Figure 4 shows the evolution of the free magnetic energy budget in NOAA AR 11158. Free energy generally follows the relative-helicity evolution, but with some notable differences. During the first four days of observations, the free magnetic energy shows a similar increase as helicity and finally peaks less than a day after the X-class flare, at the same time (decimal day 15.84). The peak energy is $\sim 6 \times 10^{32} \text{ erg}$ and is followed by a rapid $\sim 50\%$ decrease. Differences between the free energy and the relative helicity reflect the different physics of energy and helicity removal: free energy is released (dissipated) in the course of any (eruptive or confined) flare, whereas helicity is bodily removed in the course of eruptions only (excluding smaller amounts that escape by the unwinding of “open” field lines in case of interchange reconnection with helical “closed” lines). Indeed, there are occasional decreases of free magnetic energy that correspond to the energy contents of associated non-eruptive flares when helicity does not show any significant changes. A much more significant increase in free magnetic energy than helicity also occurs, immediately after the X-class flare, with an enhanced energy flux during that period, as also Figure 5 indicates. After its peak, free energy decreases with a faster ($\sim 50\%$) rate than helicity, which only drops by 30%. The initial stages of this considerable decrease, as discussed in Section 5.3.2, are due to fragmentation and large-scale magnetic field re-organization while later this decrease is the result of intense, but non-eruptive, flaring activity, as Figure 4 shows. Small-amplitude enhancements of free energy during this last day of observations coincide with similar enhancements of the energy injection rate.

Following the studied 5-day observing interval, there are still sufficient budgets of both free magnetic energy and relative helicity left in NOAA AR 11158 to further power flares

and eruptions. Indeed, as the *GOES* event catalogue indicates, two more M-class flares (M6.6 and M1.0) and 31 C-class flares occurred before the AR finally crossed the western solar limb, concluding its first disk passage. When the AR reappeared in the eastern limb (as NOAA AR 11171) it was a decaying AR with no sunspots, having two well separated, disperse opposite polarity regions and a long $H\alpha$ filament present along the PIL. The AR concluded its impressive flaring activity, according to the *GOES* event catalogue, with three more flares (M1.5, C4.5 and C6.4), occurring within a couple of days after its reappearance.

In summary, our magnetic-energy and helicity calculation can provide a plausible interpretation of the evolution in NOAA AR 11158, in qualitative agreement with independent observational and modeling/data-analysis studies. The AR builds rapidly large budgets of right-handed helicity and free energy sufficient to power several confined and eruptive flares. The overall dynamical evolution of the AR is a combination of flux emergence injecting free energy and helicity and flares/eruptions that dissipate or remove parts of these budgets. In some cases we also witness “global” (i.e., AR-wide) re-organizations of the region’s magnetic configuration. This usually follows swarms of flaring activity that affects free-energy and relative-helicity budgets. However, reorganizations occur also in the absence of flares and this may be due to fragmentation, in case flux emergence ceases, or possibly due to large-scale readjustments of the AR within the global solar magnetic field.

5.4. Energy – helicity diagram of NOAA AR 11158

Recently, Tziotziou et al. (2012) introduced the “energy-helicity” (EH) diagram of solar ARs, demonstrating a monotonic correlation between the NLFF free magnetic energy and relative magnetic helicity, as well as respective thresholds of $\sim 4 \times 10^{31}$ erg and $\sim 2 \times 10^{42}$ Mx^2 for an AR to host major (M-class and higher), generally eruptive, flares. A plausible question is whether this diagram can be reproduced by NOAA AR 11158 alone.

Figure 9 shows the compiled EH diagram for NOAA AR 11158. Magnetograms corresponding to the first 20 hours of February 12 (blue crosses), when the AR has not yet built considerable budgets of magnetic helicity and free energy (Figures 3, 4), show low, scattered values for both quantities. For this period, there also seems to exist an exponential increase of relative helicity with respect to free energy. If this behavior is real, considering of course the significant uncertainties, it would indicate that ARs tend to accumulate magnetic helicity at higher rates than free magnetic energy. However, this behavior might also be an artifact of our NLFF method that gives rise to exactly zero free energies for exactly potential fields; this is not completely guaranteed for helicity, particularly in case of existing flux imbalances (Georgoulis et al. 2012a). Concluding, it is rather difficult to disentangle between these two

different possibilities.

Once the active region has accumulated significant helicity and energy budgets (red crosses) we find that the relative helicity and free magnetic energy budgets follow quite well the derived least-squares best fit and the least-squares best logarithmic fit (Equations (3) and (4), respectively, of Tziotziou et al. 2012). This nearly monotonic dependence holds for a large range of helicities and energies. Furthermore, as Figures 3 and 4 suggest, no major flare occurs before *both* the helicity and the energy thresholds are crossed. In fact, not even C-class flares occur in the AR before these thresholds are exceeded. Once exceeded, however, a major (M-class) flare occurs within hours.

The single-AR EH diagram of Figure 9, relying solely on magnetograms from NOAA AR 11158, strongly attests to the validity of the EH diagram of Tziotziou et al. (2012). It further adds support to the conclusion that *both* magnetic free energy and helicity are important for ARs, particularly flaring ones.

5.5. Amplitudes and timing of mutual and self helicity/energy terms

As shown in Figures 3, 4 and discussed in Section 5.1, the mutual terms of the relative helicity and free energy in NOAA AR 11158 are much larger than the respective self terms. This is not a new result; Régnier et al. (2005) found from NLFF field extrapolations that the mutual helicity in NOAA AR 8210 accounts for $\sim 95\%$ of the total helicity budget. In NOAA AR 11158, mutual helicity accounts for even more of this budget: mutual-helicity terms are typically $\sim 10^3$ times larger than self-helicity terms, thus accounting for $\sim 99.9\%$ of the total helicity budget. Mutual terms in the free magnetic energy typically account for even more ($\sim 99.93\%$) of the respective budget. We find, therefore, that mutual terms caused by the interaction of different NLFF flux tubes overwhelmingly dominate the twist and writhe contributions of these flux tubes in the budgets of magnetic helicity and energy. Let us clarify at this point that the true values of the mutual-to-self helicity and energy ratios can be determined only in case of fully resolved magnetic configurations. For N discrete flux tubes (Equations (1), (2)) we have N self- and $N^2 - N$ mutual terms. Changing N due to increasing or decreasing, but always imperfect, spatial resolution, will modify the number of terms and hence the values of the ratios. In the extreme case of $N = 1$, meaning that the observing instrument resolves a single flux tube, there will be no mutual terms. The above point taken, it appears that for $N > 1$ or $N \gg 1$ independent works invariably find a clear dominance of mutual over self terms. This should be a real effect.

Another interesting result occurs when one studies the *relative timing* between mutual

and self terms of helicity and energy. This is exemplified in Figure 10, where we have normalized mutual and self terms of helicity and energy by their respective maxima. We find, then, that (i) there is a *hysteresis* in the buildup of self terms of helicity and energy with respect to these quantities’ mutual terms, and (ii) the buildup rate of self terms of helicity and energy is generally *lower* than that of the respective mutual terms, with the self-term of the free energy building up at a slightly lower rate than the self term of the relative helicity. Rough, qualitative features of the mutual-term timeseries are reproduced by self-term timeseries for both quantities, but at a delay ranging between several to ~ 24 hours. We also find remarkable coincidence in the times of peaks of mutual (helicity and energy) terms, as well as in the respective peak times of self (helicity and energy) terms. Mutual terms peak ~ 12 hours earlier than self terms.

To our knowledge, this is the first time that this result, obviously enabled by the unparalleled cadence of the SDO/HMI magnetogram data, is reported. We consider this an important finding because it attests to a possible *conversion* of mutual to self helicity and energy. More specifically, mutual interactions between an ensemble of flux tubes translate to twist and writhe of individual flux tubes of the ensemble. We cannot think of any way to achieve this, other than magnetic reconnection. Indeed, magnetic helicity is roughly conserved in the course of reconnection forcing interacting pre-reconnection flux tubes to become more helical after reconnection because they interact less than before. Naturally, this reconnection will force interaction changes to the other flux tubes of the ensemble, as well. If, however, a sequence of reconnection episodes occur in order to relax a given magnetic configuration, then the trend appears such that increasingly helical post-reconnection flux tubes are formed. The same essentially happens with free energy (more twisted structures), as well, but under the fact that energy always dissipates in the course of reconnection. These energy losses may be the reason for the slightly lower buildup rate of free energy in Figure 10.

The latter result certainly warrants further investigation. Georgoulis (2011) suggested that the small-scale flickering of numerous magnetic reconnection events occurring routinely along active-region PILs effectively transforms shear-induced mutual helicity into self helicity. The relation between PIL formation and the origin of shear has been discussed extensively by Georgoulis et al. (2012b). As a result, a new picture of pre-eruption active-region evolution appears to emerge, with typically eruptive ARs characterized by intense PILs building increasingly helical magnetic configurations along these PILs. This argument is in favor of the formation of *pre-eruption flux ropes* in ARs. Very recently, Patsourakos et al. (2013) reported direct evidence of pre-eruption flux-rope formation via a confined flare, that is obviously a magnetic reconnection episode.

5.6. Helicity and energy contents of major eruptive flares and the flare-CME connection

An admittedly untenable pursuit of relevant analyses of the past was to detect discrete, significant (i.e. beyond uncertainties) changes in free magnetic energy and relative magnetic helicity that could be related to eruptions on a case-by-case basis. Obviously this was attempted under the assumption that eruptions have energy and helicity contents that are significant fractions of the respective budgets possessed by the host AR. In this respect, Metcalf et al. (2005) were unable to determine a discrete decrease of the free magnetic energy in NOAA AR 10486 as a result of a X10 flare in the region, by applying the Virial theorem to Imaging Vector Magnetograph (IVM) data. Using vector magnetograms from the Spectropolarimeter (SP) of the Solar Optical Telescope (SOT) onboard Hinode with a cadence of a few hours, on the other hand, Georgoulis et al. (2012a) were able to estimate a change in helicity and energy of the order $5 \times 10^{42} \text{ Mx}^2$ and $2 \times 10^{32} \text{ erg}$, respectively, apparently related to a X3.4 flare triggered in NOAA AR 10930. The calculation was made as a proof of concept for the NLFF helicity and energy calculation of Section 4.1. However, given the crude cadence of the SOT/SP data, that result was handled with care.

We consider the high-cadence SDO/HMI data of this study ideal for such an investigation. Using NLFF field extrapolations, Sun et al. (2012a) detected a decrease of $\sim 3.4 \times 10^{31} \text{ erg}$ after the X2.2 flare of 2011 February 15 in NOAA AR 11158. In this study we attempt to detect changes in both free magnetic energy and relative magnetic helicity. Moreover, we do not restrict the analysis to the X-class flare alone: instead, we study the helicity and free-energy evolution in the course of the four (4) largest eruptive flares in NOAA AR 11158 during the 5-day observing interval. The results are shown in Figure 11 and are overplotted on co-temporal *Wind*/WAVES frequency-time spectra for reference. All shown curves are 72-minute averages. Given the small uncertainties in helicity and free energy (Figures 3, 4), all notable changes that last much longer than the HMI cadence of 12 minutes should be considered significant and stemming purely from changes in the calculated connectivity matrices.

Figure 11 leads us to three major conclusions: first, in at least three of the four eruptive flares studied (Figure 11a, c, and d) there is a significant decrease in the magnitudes of the AR’s relative helicity and free energy. Second, and perhaps more importantly, these decreases start occurring *well before* the onset of the flare and the projected launch time of the associated CME. Third, decreases are not instantaneous but *transient*, lasting for 2 – 3 hours. Flares and CMEs occur toward the end (15 – 30 minutes before the end) of these dips. After the end of the dips, the relative-helicity and free-energy budgets follow the underlying, general trends of these budgets for the period of interest.

The properties of the relative-helicity and free-energy decreases, including properties of the four eruptive flares, are summarized in Table 1. The peak amplitude of the helicity and energy decreases in Figure 11 is viewed as the respective helicity and energy contents of the associated eruption. In this respect, the eruption related to the X2.2 flare (Figure 11a) has an energy content of $\sim 8.4 \times 10^{31}$ erg, a factor of <3 larger than the estimate of Sun et al. (2012a). The helicity budget of the respective CME is $\sim 2.6 \times 10^{42} Mx^2$, in excellent agreement with estimated typical helicity contents of CMEs (DeVore 2000; Georgoulis et al. 2009). The other three eruptions are associated with energy releases of the order 10^{31} erg to several times this budget. For the eruptions related to the M2.2 and M1.6 flares (Figures 11c, 11d, respectively) the helicity content of the CMEs stays close to $2 - 3 \times 10^{42} Mx^2$. For the eruption associated to the M6.6 flare (Figure 11b), however, it is an order-of-magnitude smaller $\sim 3 \times 10^{41} Mx^2$. We are unclear on why this CME is so much weaker but this is corroborated by the facts that (i) the CME shock appears rather weak in *Wind*/WAVES spectra (at least weaker than the others in Figures 11a, c, and d), and (ii) the LASCO CME catalog has registered this CME as “Poor” and “Partial Halo”.

In an attempt to explain why we observe these decreases in the AR’s relative helicity and free energy prior to major eruptive flares, we construct in Figure 12 the respective timeseries for the total connected flux Φ_{conn} (i.e., the flux participating in the connectivity matrix), the total “open” flux Φ_{open} (i.e., the flux closing beyond the bounds of the AR), and the number of flux tubes participating in the connectivity matrix. Figure 12 shows that co-temporal with helicity/energy decreases are *slight decreases* in the connected flux Φ_{conn} for all four eruptive flares. The most significant of these decreases pertains to the X2.2 flare and associated eruption ($\sim 6\%$; Figures 11a, 12a) while the least significant pertains to the M6.6 flare with the weakest CME ($\sim 0.7\%$; Figures 11b, 12b). These decreases do not seem to be associated with respective increases in the “open” flux Φ_{open} (except, perhaps, a very slight increase in Figure 12c); this would mean that previously “closed” connections, i.e., connections with both ends within the AR, now close beyond it. Instead, these decreases imply that the normal field component B_z that determines the connected flux becomes somewhat *weaker* prior to the eruptions. This is in line with multiple recent works that advocate for (Fisher et al. 2012; Hudson et al. 2012) or report (Petrie 2012; Sun et al. 2012a) enhancements in the horizontal magnetic field and slighter decreases in the normal field component. Those arguments and findings mainly refer to the photospheric vicinity of the eruption but, as we can see from Figure 12, they are also detectable over the entire AR. However, our results do not support an irreversible or permanent decrease of the connected flux; in this respect, our results run counter to those works advocating irreversibility, at least in terms of a B_z -decrease. Point taken, notice that Sun et al. (2012a) did not find an unambiguously irreversible B_z -decrease in the case of the X2.2 flare in NOAA AR 11158.

Thanks to the unprecedented cadence of the SDO/HMI magnetogram data, our results help clarify an additional crucial point: so far the above eruption-related flux changes were confirmed by inspecting the pre- and post-eruption configurations. Here we deduce that flux-decreases occur mostly *prior* to eruptions, with the eruptions themselves occurring either at the last stages of these decreases or shortly thereafter. This is sound evidence toward resolving the elusive flare-CME connection: from our results, the unstable magnetic structure that will evolve to become a CME starts ascending *clearly* before the flare and the a-posteriori projected CME launch time. To our understanding, this is the only possibility that can interpret the connected-flux decreases as changes in the Lorentz force, but also as contraction / collapse of pre-eruption loops as the CME progenitor increases in size and ascends faster (Vourlidas et al. 2012). The flare is a result of the drastic perturbation caused by this ascension. Notice that this interpretation has appeared also in earlier works (Zhang & Dere 2006) but only now has this picture been clearly supported by independent observational, modeling, and theoretical works.

The present study includes only a limited sample of eruptive flares. In followup works we will further test our findings with larger flare samples and aim to compare results between eruptive and confined flares.

6. Discussion and conclusions

The magnetic free energy and relative magnetic helicity budgets in NOAA AR 11158 have been studied using high-cadence, constant-quality, space-based vector magnetograms acquired by the HMI magnetograph onboard SDO. Budgets have been derived using the novel NLFF method introduced by Georgoulis et al. (2012a) that requires *single* photospheric (or chromospheric) vector magnetograms. The constructed timeseries of budgets for free energy and relative helicity comprise of values independent from each other. For reference, we use energy and helicity budgets obtained by time-integration of energy and helicity injection rates, respectively, inferred using the DAVE4VM photospheric flow field. Successive points in the budget timeseries are related to each-other in this case. The only alternative way to infer magnetic energy and helicity budgets is by (NLFF, preferably) magnetic-field extrapolations, relying also on single vector magnetograms and hence providing independent budgets in the timeseries. However, both extrapolations and energy/helicity fluxes require additional nontrivial information in order to yield energy and helicity budgets (see Introduction). Much of this information, particularly the NLFF-extrapolated and the velocity fields, are strongly

model-dependent[†]. Therefore, if we can show that our method reliably calculates energy and helicity budgets at a given AR without requiring information other than this AR’s vector magnetogram, then this or refined future techniques of this kind might become methods of choice for the task at hand.

Keeping in mind that the rate-integrated helicity and energy budgets do not share the same physical meaning with our instantaneous budgets, we find a qualitative correspondence between the two (Section 5.2). Indeed, the peak of the integrated helicity in the region is $\sim 2.5 \times 10^{43} \text{ Mx}^2$ while our instantaneous budget shows a peak $\sim 2 \times 10^{43} \text{ Mx}^2$. The total energy budget from our method, on the other hand, peaks at $\sim 1.6 \times 10^{33} \text{ erg}$, while the peak of the flux-integrated budget is lower, $\sim 9 \times 10^{32} \text{ erg}$. The morphologies of the two timeseries are different due to their different physical origins and meaning. This being said, our NLFF field energy and helicity budgets depend more sensitively on the AR’s eruptive and non-eruptive evolution. We conclude, therefore, that NLFF methods such as the one implemented here are indeed important for decoding the dynamical evolution of ARs from high-cadence vector magnetogram data.

Stepping on this central conclusion, our analysis has led to a meaningful interpretation of the evolution and the eruptive activity of NOAA AR 11158. Besides free magnetic energy, analysis provides further evidence that magnetic helicity is, indeed, an important ingredient of the overall evolution in solar ARs.

The attained budgets of free magnetic energy and relative helicity in NOAA AR 11158 imply clearly that the AR builds up *both* significant amounts of energy and dominant (in this case positive [right-handed]) helicity before entering major flaring and eruptive territory. Our method only shows the increases in the energy/helicity budgets without providing a rigorous physical investigation of why this happens except, of course, the increasing size and complexity of the magnetic connectivity matrix that is fuelled by continuous flux emergence in the AR (Figure 2). Previous observational works that reported shearing motions along the AR’s PIL and rotating sunspots (Section 3) complement the picture and our results. The AR hosts major eruptions when both previously inferred free-energy and relative-helicity thresholds, $4 \times 10^{31} \text{ erg}$ and $2 \times 10^{42} \text{ Mx}^2$, respectively, are exceeded (Tziotziou et al. 2012). In addition, the constructed – from the 600 magnetograms of this AR alone – EH diagram clearly follows and further validates the monotonic correlation between the two quantities found by Tziotziou et al. (2012) from the study of 42 ARs (Section 5.4).

[†]Our choice for the DAVE4VM velocity field relies on studies that this velocity field, consistent with the MHD induction equation, is one of the most credible choices for the photosphere (Welsch et al. 2007; Scherrer et al. 2012).

Superposed on the overall increasing tendency of free-energy and relative-helicity budgets throughout the 5-day observing interval are prolonged, significant decreases of these budgets that last for several hours. We have identified two different reasons for these dips: first, a “large-scale”, AR-wide re-organization of the magnetic configuration and, second, confined/eruptive flaring activity in the AR.

An AR-wide re-structuring that results in energy/helicity decreases manifests itself via (i) a decrease of the connected flux Φ_{conn} participating in the connectivity matrix, accompanied by an increase of the respective “open” magnetic flux Φ_{open} , or (ii) an increase of the number of active connections (thought as slender flux tubes) accompanied by a decrease in Φ_{conn} (Figures 6, 8). In the first case, flux closing within the AR up until a certain time now closes beyond its limits. As “open” flux is not currently included in our energy/helicity calculations, this results in a decrease of the calculated budgets. In the second case, the AR fragments to more partitions at smaller Φ_{conn} leading to the same net result.

An eruption in the AR, on the other hand, will result in a temporarily smaller Φ_{conn} , apparently due to the eruption-related weakening of the normal-field component (Section 5.6). This has been attributed to the action of the Lorentz force in the eruption area and is supported by observations. However, the new result in our case is that the weakening occurs *before* the observed onset of the eruption, i.e. the flare onset and/or the projected CME launch time. We interpret this finding as solid evidence that the CME progenitor starts ascending well before the flare. This sheds light on the elusive flare-CME connection and interprets flares as consequences of the CME-progenitor destabilization, rather than as triggers of this destabilization. This behavior is clearly seen in three out of four major eruptive flares the AR hosted within the observing interval. In the remaining eruptive flare the AR exhibited qualitatively the same behavior but to a much smaller extent. The most conspicuous decrease of Φ_{conn} was $\sim 6\%$ and was associated with the X2.2 flare of 2011 February 15, giving rise to a helicity content of the CME of the order $2.6 \times 10^{42} \text{ Mx}^2$ and an energy content for the eruption as a whole of the order $8.4 \times 10^{31} \text{ erg}$. If similar results are confirmed, and we plan to carry out follow-up studies of this type, we envision a routine calculation of eruption energetics and helicity in the future. At the moment, nevertheless, it appears safe to conclude that ARs possess much higher free energy and helicity budgets than those of the largest eruptions they may ever host. When this is no longer valid, the AR in question has already entered the final decay phase that will result in its demise.

Another finding of this study was that eruption-related energy and helicity decreases are not irreversible or permanent but transient and restored within several hours by the general trend of the budgets in the AR. The interpretation of this effect, especially in view of works that show permanent decreases of B_z and/or increases of the horizontal field, remains to be

investigated.

A further important finding that corroborates the credibility of our calculations is the AR’s evolution during the last day of the observing interval. Activity in the AR on 2011 February 16 was characterized by repeated but *confined* flaring activity, lacking conspicuous CMEs. Monitoring the free magnetic energy of the AR (Figure 4) we notice a nearly monotonic decrease by $\sim 3 \times 10^{32}$ erg within less than a day, mostly due to energy dissipation in the course of repeated flaring. The relative helicity, however, fluctuates around a well-defined mean value of $\sim 1.5 \times 10^{43}$ Mx² (Figure 3) due to its rough conservation in the course of the confined flares. Such different behavior stemming from the core properties of magnetic free energy and relative magnetic helicity accounts for nonlinearities in the EH diagram of solar ARs.

Concluding, we underline the new, emerging picture of the pre-eruption evolution in ARs that our results have enabled and previous studies have envisioned: this picture relies on the timing between mutual- and self-terms of free energy and relative helicity. We find a significant (much larger than the observational cadence) *hysteresis* of self-term development in comparison to mutual terms that are developed earlier and at higher buildup rates (Section 5.5). We consider this evidence of a mutual-to-self *conversion* of energy and helicity, rather than an independent, out-of-phase buildup of both. Moreover, the higher buildup rate of self-helicity compared to the respective rate of the self-free-energy, in view also of the rough conservation of helicity in an isolated, non-eruptive magnetic structure points to a simple (and single) interpretation of this conversion: *magnetic reconnection*. The most profound reconnection area of an AR is its PIL(s); the stronger the PIL, the more intense the flickering of magnetic reconnection along it. Reconnection along intense PILs is due to the action of shear that adds stresses to the already complex magnetic configuration, while shear is caused by Lorentz force that acts along the PIL and only there (Georgoulis et al. 2012b). As hinted by Georgoulis (2011) and shown here more convincingly, this logical, hierarchical sequence of dynamical evolution results in increasingly helical magnetic structures as PIL evolves. Otherwise put, this may well be independent evidence in favor of pre-eruption helical flux-rope formation that was hypothesized, theorized, or observationally reported by multiple previous works. We plan to further elucidate this result in future follow-up studies.

We are grateful to P.W. Schuck for valuable, extensive discussions pertaining to DAVE4VM and its application to this data set. The data are used courtesy of NASA/SDO and the HMI science team. YL was supported by NASA Contract NAS5-02139 (HMI) to Stanford University. This work was supported from the EU’s Seventh Framework Programme under grant agreement n° PIRG07-GA-2010-268245.

REFERENCES

- Alvarado-Gómez, J. D., Buitrago-Casas, J. C., Martínez-Oliveros, J. C., et al. 2012, *Sol. Phys.*, 280, 335
- Aschwanden, M. J., Boerner, P., Schrijver, C. J., & Malanushenko, A. 2011, *Sol. Phys.*, 384
- Beauregard, L., Verma, M., & Denker, C. 2012, *Astronomische Nachrichten*, 333, 125
- Berger, M. A. 1984, Ph.D. Thesis, Harvard Univ.
- Berger, M. A. 1999, *Plasma Physics and Controlled Fusion*, 41, 167
- Berger, M. A., & Field, G. B. 1984, *Journal of Fluid Mechanics*, 147, 133
- Borrero, J. M., Tomczyk, S., Kubo, M., et al. 2011, *Sol. Phys.*, 273, 267
- Bougeret, J.-L., Kaiser, M. L., Kellogg, P. J., et al. 1995, *Space Sci. Rev.*, 71, 231
- Canfield, R. C., Hudson, H. S., & McKenzie, D. E. 1999 *Geophys. Res. Lett.*, 26, 627
- Chae, J. 2001, *ApJ*, 560, L95
- Démoulin, P., & Berger, M. A. 2003, *Sol. Phys.*, 215, 203
- Démoulin, P., Pariat, E., & Berger, M. A. 2006, *Sol. Phys.*, 233, 3
- DeVore, C. R. 2000, *ApJ*, 539, 944
- Finn, J. M., & Antonsen, T. M., Jr. 1988, *Plasma Phys. Controlled Fusion*, 9, 111
- Fisher, G. H., Bercik, D. J., Welsch, B. T., & Hudson, H. S. 2012, *Sol. Phys.*, 277, 59
- Freedman, M. H. & Berger, M. A. 1993, *Geophys. Astrophys. Fluid Dyn.*, 73, 91
- Gary, G. A., & Hagyard, M. J. 1990, *Sol. Phys.*, 126, 21
- Georgoulis, M. K. 2005, *ApJ*, 629, L69
- Georgoulis, M. K. 2011, *IAU Symposium*, 273, 495
- Georgoulis, M. K. 2012, *Sol. Phys.*, 276, 423
- Georgoulis, M. K. & LaBonte, B. J. 2007, *ApJ*, 671, 1034
- Georgoulis, M. K., & Rust, D. M. 2007, *ApJ*, 661, L109

- Georgoulis, M. K., Rust, D. M., Pevtsov, A. A., Bernasconi, P. N., & Kuzanyan, K. M. 2009, *ApJ*, 705, L48
- Georgoulis, M. K., Titov, V. S., & Mikić, Z. 2012b, *ApJ*, 761, 61
- Georgoulis, M. K., Tziotziou, K., & Raouafi, N.-E. 2012a, *ApJ*, 759, 1
- Gibson, S. E., Fan, Y., Török, T., & Kliem, B. 2006 *Space Sci. Rev.*, 124, 131
- Gosain, S. 2012, *ApJ*, 749, 85
- Hillan, D. S., Cairns, I. H., & Robinson, P. A., 2012, *J. Geophys. Res.*, 117, A3, CiteID A03104
- Hudson, H. S., Fletcher, L., Fisher, G. H., Abbett, W. P., & Russell, A. 2012, *Sol. Phys.*, 277, 77
- Jiang, Y., Zheng, R., Yang, J., et al. 2012, *ApJ*, 744, 50
- Jing, J., Park, S.-H., Liu, C., et al. 2012, *ApJ*, 752, L9
- Kumar, P., Cho, K.-S., Bong, S.-C., Park, S.-H., & Kim, Y. H. 2012, *ApJ*, 746, 67
- Kusano, K., Maeshiro, T., Yokoyama, T., & Sakurai, T. 2002, *ApJ*, 577, 501
- LaBonte, B. J., Georgoulis, M. K., & Rust, D. M. 2007, *ApJ*, 671, 955
- Liu, Y., Zhao, J., & Schuck, P. W. 2012a, *Sol. Phys.*, doi: 10.1007/s11207-012-0089-3
- Liu, Y., & Schuck, P. W. 2012, *ApJ*, 761, 105
- Liu, C., Deng, N., Liu, R., et al. 2012b, *ApJ*, 745, L4
- Low, B. C. 1994, *Physics of Plasmas*, 1, 1684
- Maurya, R. A., Vemareddy, P., & Ambastha, A. 2012, *ApJ*, 747, 134
- Metcalf, T. R., Leka, K. D., & Mickey, D. L., 2005, *ApJ*, 623, L53
- Metcalf, T. R., Leka, K. D., Barnes, G., et al. 2006, *Sol. Phys.*, 237, 267
- Metcalf, T. R., De Rosa, M. L., Schrijver, C. J., et al. 2008, *Sol. Phys.*, 247, 269
- Nindos, A., & Andrews, M. D. 2004, *ApJ*, 616, L175

- Nindos, A. 2009, in IAU Symp. 257, Universal Heliophysical Processes (Cambridge: Cambridge Univ. Press), 133
- Nindos, A., Patsourakos, S., & Wiegmann, T. 2012, ApJ, 748, L6
- November, L. J., & Simon, G. W. 1988, ApJ, 333, 427
- Pariat, E., Antiochos, S. K., & DeVore, C. R. 2009, ApJ, 691, 61
- Patsourakos, S., Vourlidas, A., & Stenborg, G. 2013, ApJ, 764, 125
- Pesnell, W. D., Thompson, B. J., & Chamberlin, P. C. 2012, Sol. Phys., 275, 3
- Petrie, G. J. D. 2012, Sol. Phys., doi:10.1007/s11207-012-0071-0
- Phillips, A. D., MacNeice, P. J., & Antiochos, S. K. 2005, ApJ, 624, L129
- Raouafi, N.-E., Georgoulis, M. K., Rust, D. M., & Bernasconi, P. N. 2010, ApJ, 718, 981
- Regnier, S., Amari, T., & Canfield, R. C., 2005, A&A, 442, 345
- Rust, D. M. & LaBonte, B. J. 2005, ApJ, 622, L69
- Scherrer, P. H., Schou, J., Bush, R. I., et al. 2012, Sol. Phys., 275, 207
- Schrijver, C. J. 2009, Advances in Space Research, 43, 739
- Schrijver, C. J., De Rosa, M. L., Metcalf, T. R., et al. 2006, Sol. Phys., 235, 161
- Schrijver, C. J., Aulanier, G., Title, A. M., Pariat, E., & Delannée, C. 2011, ApJ, 738, 167
- Schuck, P. W. 2005, ApJ, 632, L53
- Schuck, P. W. 2006, ApJ, 646, 1358
- Schuck, P.W. 2008, ApJ, 683, 1134
- Smyrli, A., Zuccarello, F., Romano, P., et al. 2010, A&A, 521, A56
- Song, Q., Zhang, J., Yang, S., & Liu, Y. 2012, arXiv:1209.6192
- Sun, X., Hoeksema, J. T., Liu, Y., et al. 2012a, ApJ, 748, 77
- Sun, X., Hoeksema, J. T., Liu, Y., Chen, Q., & Hayashi, K. 2012b, ApJ, 757, 149
- Török, T., & Kliem, B. 2005, ApJ, 630, L97

- Tziotziou, K., Georgoulis, M. K., & Raouafi, N.-E. 2012, *ApJ*, 759, L4
- Vemareddy, P., Ambastha, A., Maurya, R. A., & Chae, J. 2012a, *arXiv:1202.5195*
- Vemareddy, P., Ambastha, A., & Maurya, R. A. 2012b, *ApJ*, 761, 60
- Vourlidas, A., Syntelis, P., & Tsinganos, K. 2012, *Sol. Phys.*, 280, 509
- Wang, S., Liu, C., Liu, R., et al. 2012, *ApJ*, 745, L17
- Welsch, B. T., Abbett, W. P., De Rosa, M. L., et al. 2007, *ApJ*, 670, 1434
- Zhang, J. & Dere, K. P. 2006, *ApJ*, 649, 1100
- Zuccarello, F. P., Jacobs, C., Soenen, A., et al. 2009, *A&A*, 507, 441

No	Date	Decrease Properties			Flare Properties		ΔH_m (Mx^2)	ΔE_c (erg)
		Start	Peak	End	Onset	Class		
1	15-Feb-2011	23:22 [†]	00:13	02:00	01:44	X2.2	2.6×10^{42}	8.4×10^{31}
2	13-Feb-2011	16:25	16:50	18:10	17:28	M6.6	2.9×10^{41}	1×10^{31}
3	14-Feb-2011	15:35	16:25	17:50	17:20	M2.2	2.8×10^{42}	4.9×10^{31}
4	16-Feb-2011	11:13	12:35	13:44	14:19	M1.6	2×10^{42}	6.5×10^{31}

Table 1: Temporal properties of the calculated decrease in relative magnetic helicity and free magnetic energy in NOAA AR 11158 for the four largest eruptive flares that occurred in the AR during the observing interval. The estimated eruption-related peak decreases ΔH_m and ΔE_c are also provided. All times are universal times. Helicity and energy values have been obtained by the 72-minute average timeseries of the respective quantities (Figures 3, 4, respectively).

[†]On 14-Feb-2011

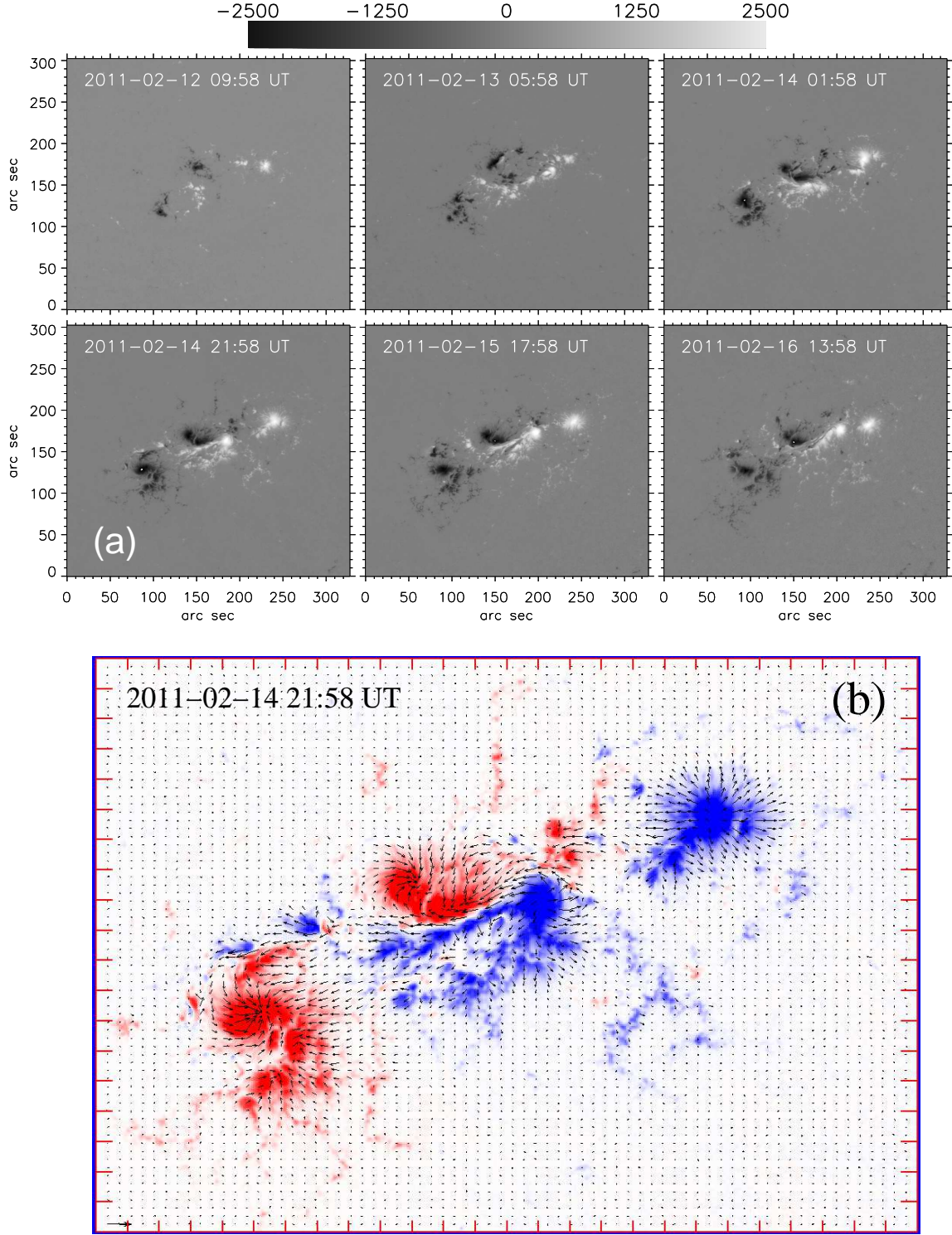


Fig. 1.— (a) Sequence of the heliographic vertical field component (B_z) in NOAA AR 11158, as acquired by SDO/HMI. (b) Detailed vector magnetogram corresponding to the fourth snapshot of the sequence, with B_z saturated at ± 1500 G. The vector in the lower-left edge corresponds to a horizontal magnetic field of 2000 G. For all images, north is up and west is to the right.

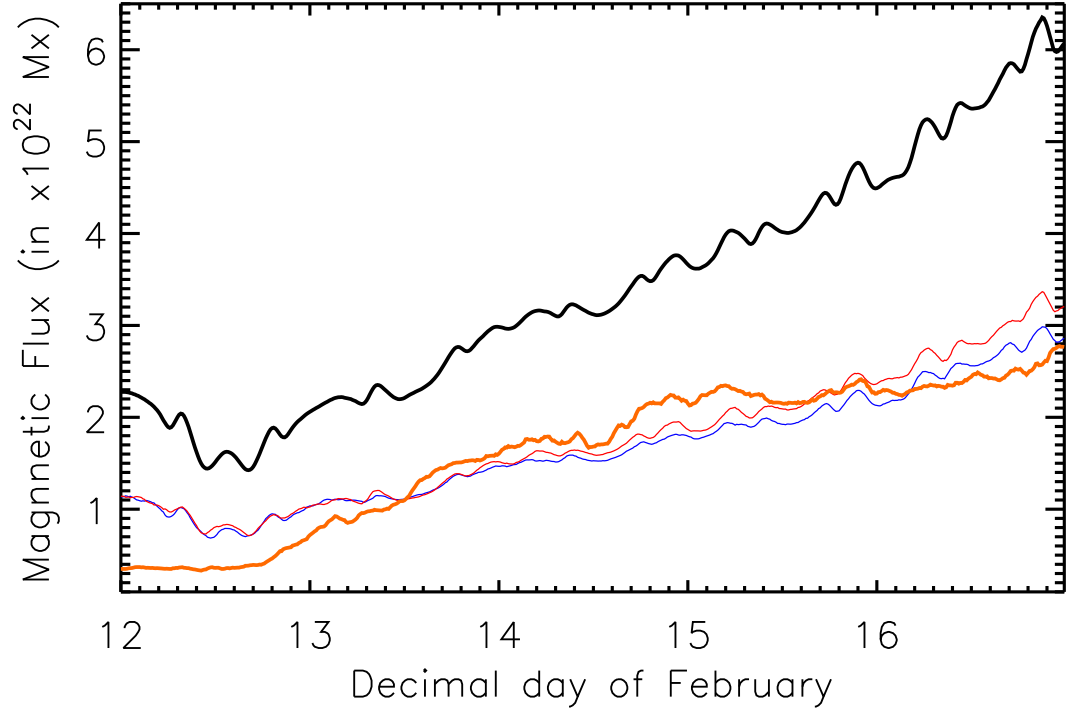


Fig. 2.— Evolution of magnetic flux budgets in NOAA AR 11158. The unsigned (total flux) is shown by the black curve. The magnitudes of positive- and negative-polarity fluxes are shown by the red and blue curves, respectively. The unsigned flux participating in the magnetic connectivity matrix in the AR (see Section 4.1 for details) is shown by the orange curve. For clarity in assessing the long-term evolution of the AR, all shown curves are 72-minute averages of the actual curves.

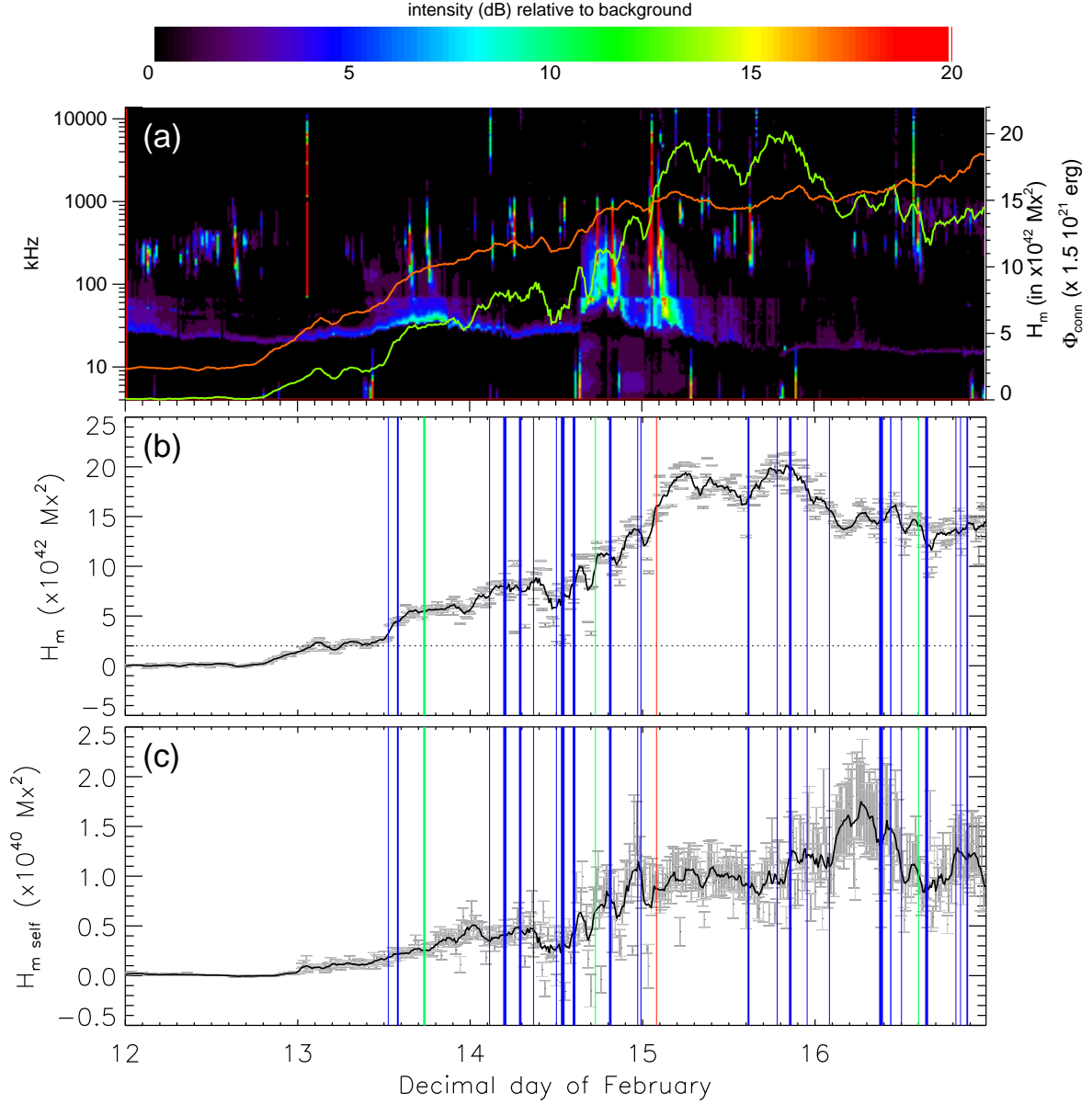


Fig. 3.— (a) 72-minute averages of the resulting NLFF relative magnetic helicity H_m (green curve) and unsigned connected magnetic flux Φ_{conn} (orange curve), overplotted on a frequency-time *Wind*/WAVES radio spectrum for the 5-day observing interval. (b) 72-minute average H_m (solid curve) and actual H_m (grey symbols and error bars) for the same observing interval. Notice that H_m is indistinguishable from its mutual term $H_{m \text{ mut}}$ due to the small magnitude of its self term $H_{m \text{ self}}$. (c) 72-minute average $H_{m \text{ self}}$ (solid curve) and actual $H_{m \text{ self}}$ (grey symbols and error bars). Vertical blue, green, and red lines in (b) and (c) denote the peak times of C-, M-, and X-class flares, respectively, with their thickness roughly corresponding to the magnitude of the given flare class. The dotted horizontal line in (b) indicates the $\sim 2 \times 10^{42} \text{ Mx}^2$ threshold for relative magnetic helicity (see text and Tziotziou et al. 2012).

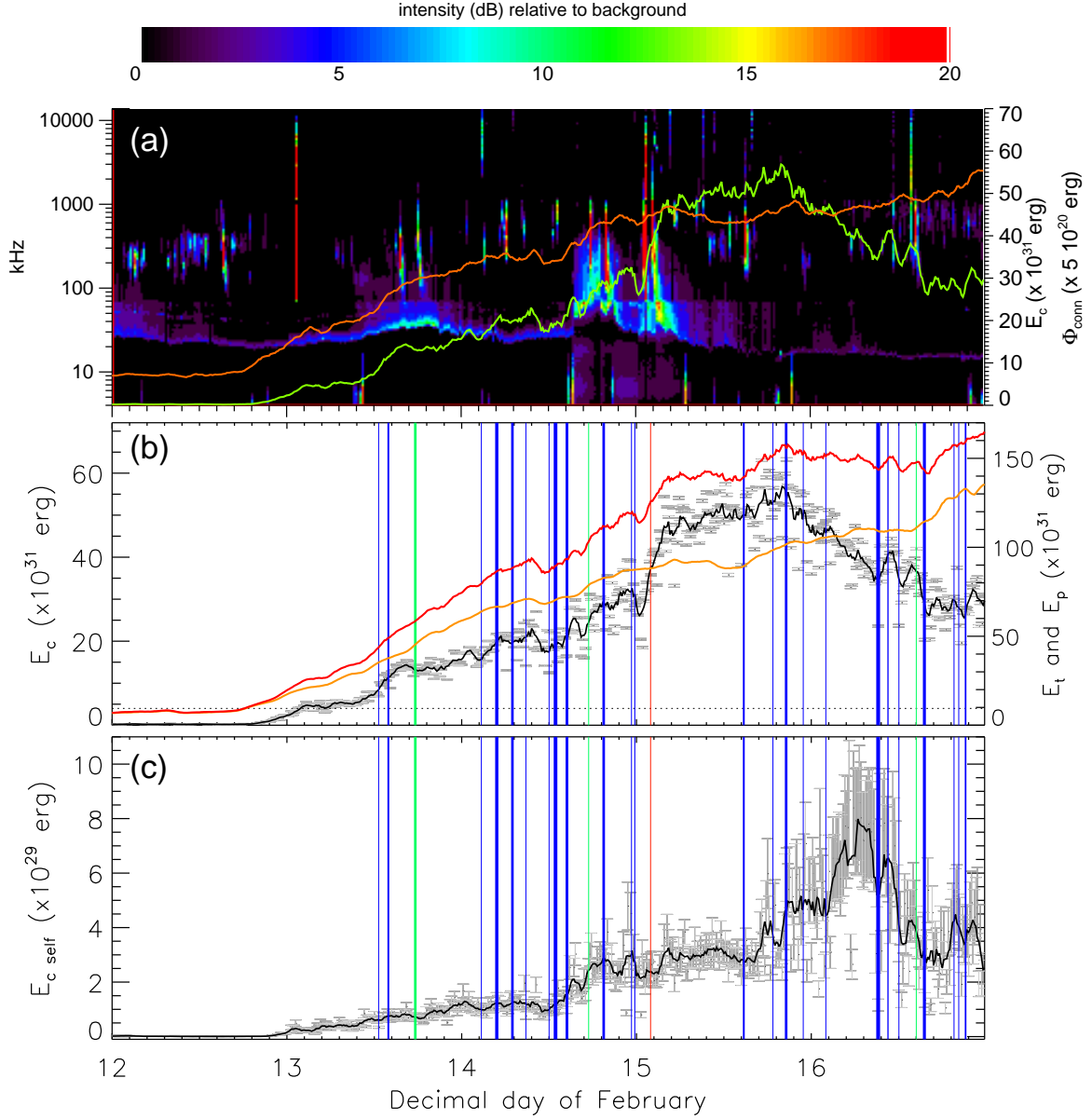


Fig. 4.— (a) 72-minute averages of the resulting NLFF free magnetic energy E_c (green curve) and unsigned connected magnetic flux Φ_{conn} (orange curve), overplotted on a frequency-time *Wind*/WAVES radio spectrum for the 5-day observing interval. (b) 72-minute average E_c (solid black curve) and actual E_c (grey symbols and error bars) for the same observing interval. The reference (potential) and total magnetic energy, E_p and E_t , respectively, are shown by the yellow and red curves, respectively. Notice that E_c is indistinguishable from its mutual term $E_{c_{\text{mut}}}$ due to the small magnitude of its self term $E_{c_{\text{self}}}$. (c) 72-minute average $E_{c_{\text{self}}}$ (solid curve) and actual $E_{c_{\text{self}}}$ (grey symbols and error bars). Vertical blue, green, and red lines in (b) and (c) denote the peak times of C-, M-, and X-class flares, respectively, with their thickness roughly corresponding to the magnitude of the given flare class. The dotted horizontal line in (b) indicates the $\sim 4 \times 10^{31}$ erg threshold for free magnetic energy (see text and Tziotziou et al. 2012).

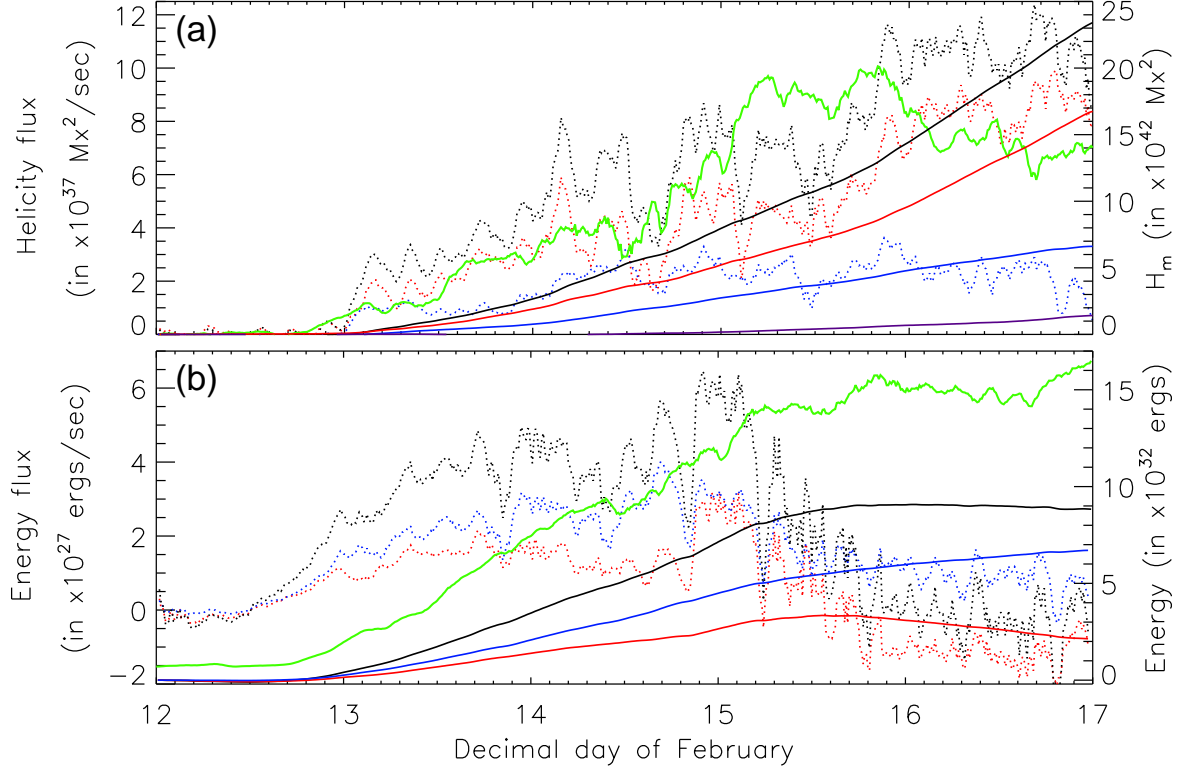


Fig. 5.— 72-minute average temporal profiles of the relative-magnetic-helicity (a) and the total-magnetic-energy (b) fluxes and their integrated budgets. Dotted red, blue, and black lines correspond to the shuffling-, emergence-, and total-flux terms, respectively (readings on left ordinate). The respective integrated budgets as a function of time are given by solid red, blue, and black lines (readings on right ordinate). For reference, our NLFF relative helicity budget (a) and total energy budget (b) are also given by the green curves (readings on right ordinate). The thick purple line in (a) shows the accumulated emergence helicity inferred using a LCT velocity (see text).

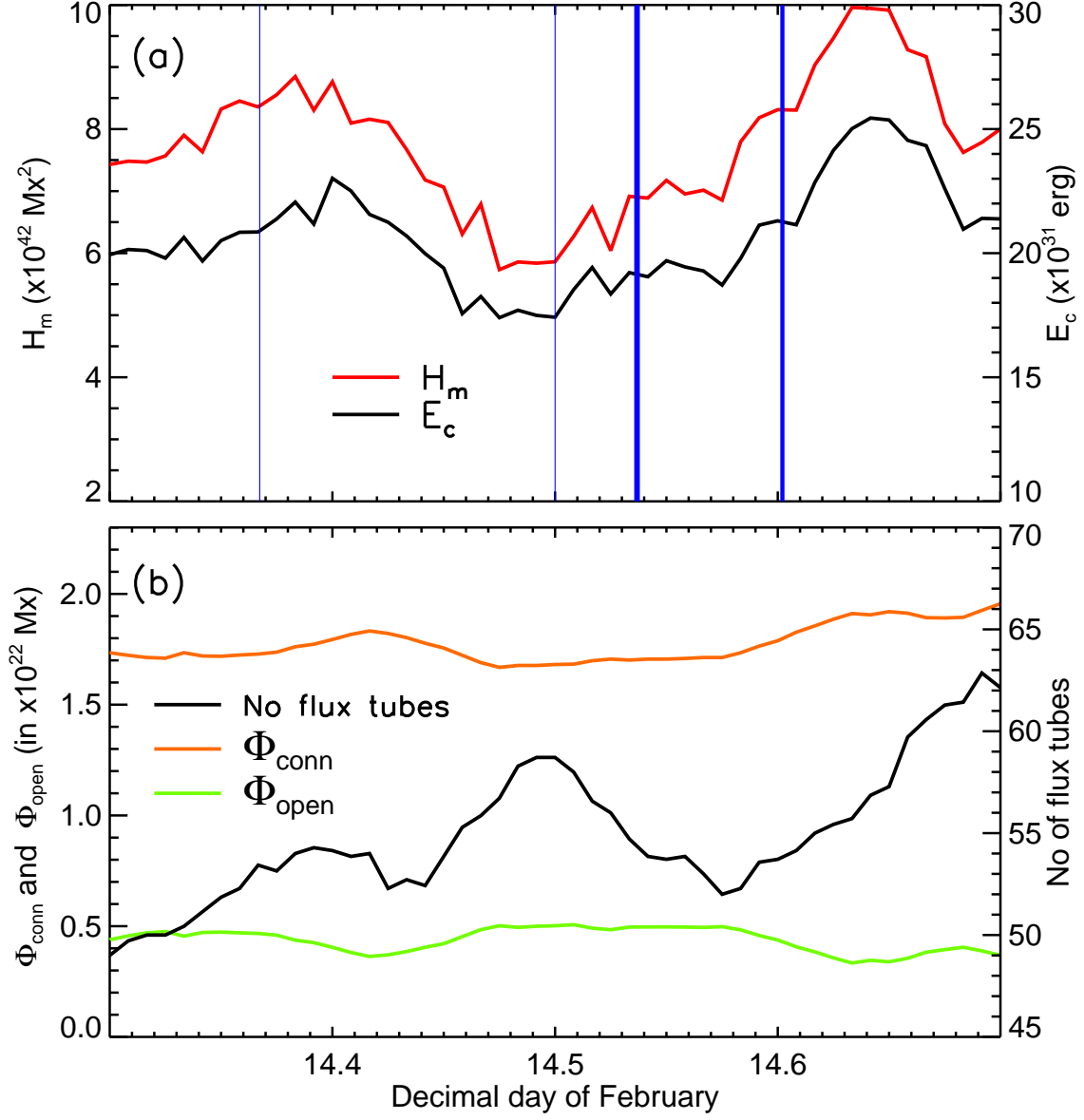


Fig. 6.— 72-minute average temporal profiles of (a) relative magnetic helicity and free magnetic energy, and (b) unsigned connected flux Φ_{conn} , open flux Φ_{open} and number of flux tubes participating in the connectivity matrix around midday on 2011 February 14. Vertical blue lines in (a) denote the peak times of C-class flares with their thickness roughly corresponding to the flare magnitude.

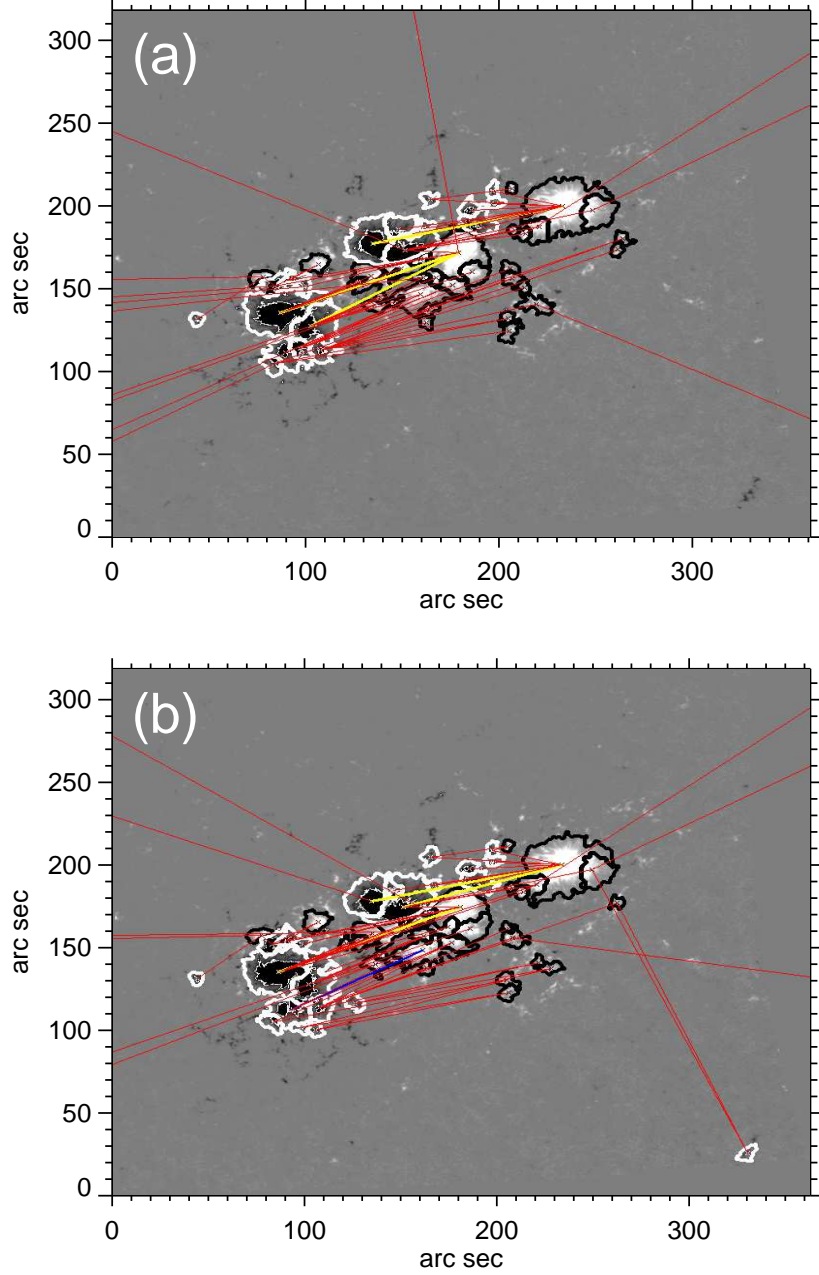


Fig. 7.— Magnetic connectivity in NOAA AR 10254, observed on February 15, 01:24 UT (a) before the onset of the X2.2 flare and on February 15, 02:24 UT (b) after the flare. Images show the vertical magnetic field component in gray scale with the contours bounding the identified magnetic partitions. The flux-tube connections identified by the magnetic connectivity matrix are represented by line segments connecting the flux-weighted centroids of the respective pair of partitions. Red, cyan, and yellow segments denote magnetic flux contents within the ranges $[5 \times 10^{19}, 5 \times 10^{20}]$ Mx, $[5 \times 10^{20}, 10^{21}]$ Mx, and $[10^{21}, 5 \times 10^{21}]$ Mx, respectively. Both closed and “open”, i.e. closing beyond the AR’s limits, connections are shown. North is up; west is to the right.

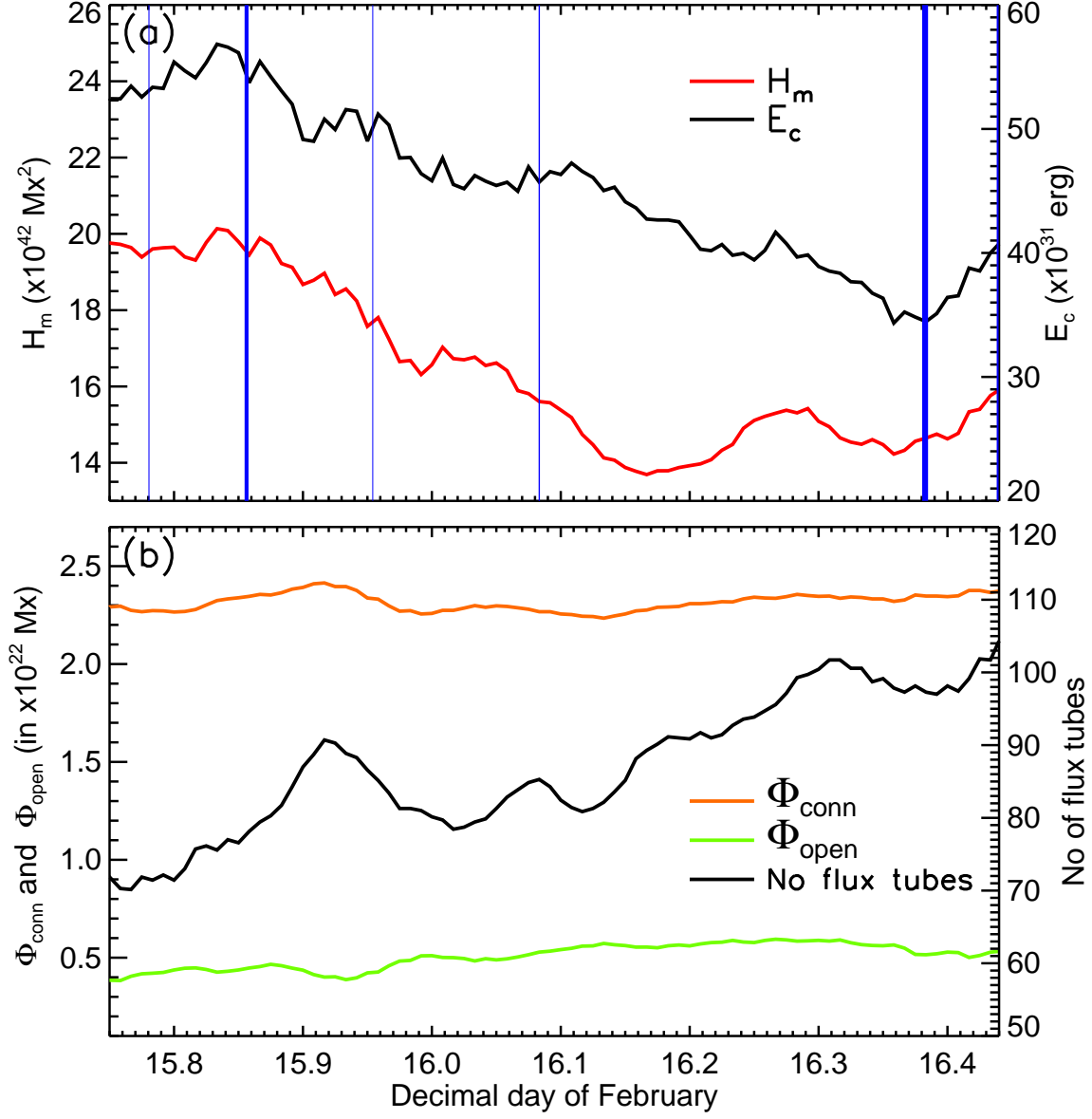


Fig. 8.— 72-minute average temporal profiles of (a) relative magnetic helicity and free magnetic energy, and (b) unsigned connected flux Φ_{conn} , open flux Φ_{open} and number of flux tubes participating in the connectivity matrix between late February-15 and early February-16. Vertical blue lines in (a) denote the peak times of C-class flares with their thickness roughly corresponding to the flare magnitude.

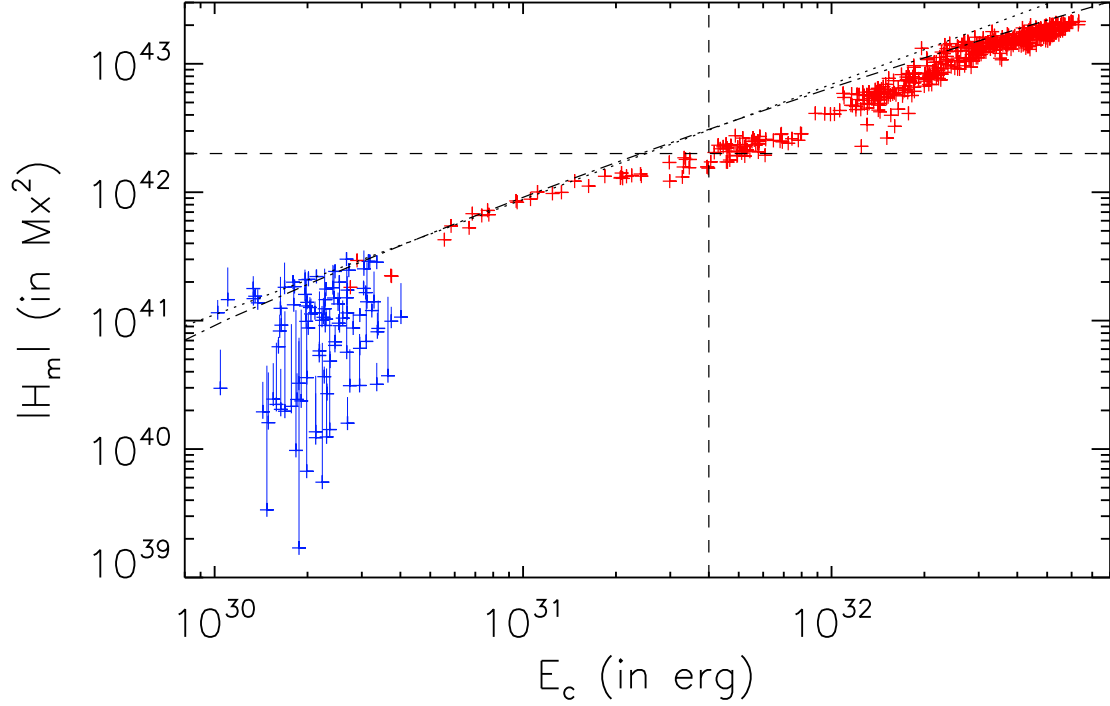


Fig. 9.— The energy-helicity diagram for NOAA AR 11158, comprising of the AR’s free magnetic energy and the respective magnitude of the relative magnetic helicity. Blue crosses indicate energy and helicity values for the first 20 hours of 2011 February 12 (see text), while error bars for the absolute relative helicity (only to higher values) are indicated with blue lines. Dashed lines indicate the previously estimated thresholds for relative magnetic helicity ($\sim 2 \times 10^{42} \text{ Mx}^2$) and free magnetic energy ($\sim 4 \times 10^{31} \text{ erg}$) above which ARs host major flares (Tziotziou et al. 2012). The dotted and dash-dotted lines denote the derived least-squares best fit and the least-squares best logarithmic fit of Tziotziou et al. (2012) (Equations (3) and (4), respectively, of that work).

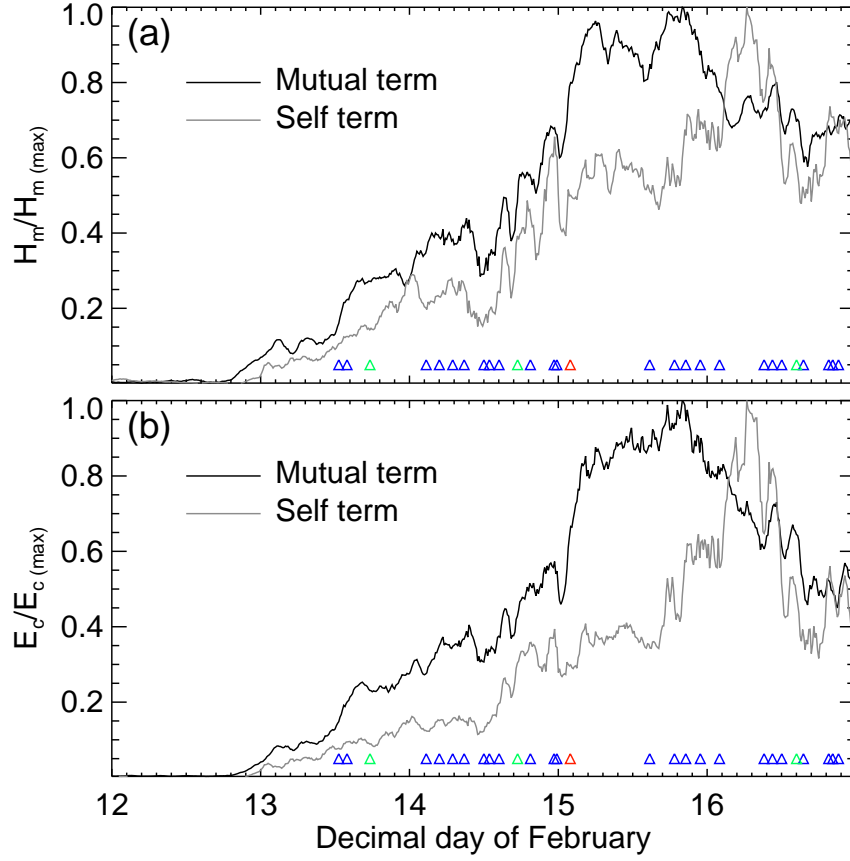


Fig. 10.— Timeseries of the normalized – with respect to its maximum – mutual (black) and self (grey) terms of the relative magnetic helicity (a) and free magnetic energy (b) in NOAA AR 11158. Colored triangles denote the onset times of flares in the AR, with blue, green, and red denoting C-, M-, and X-class flares, respectively.

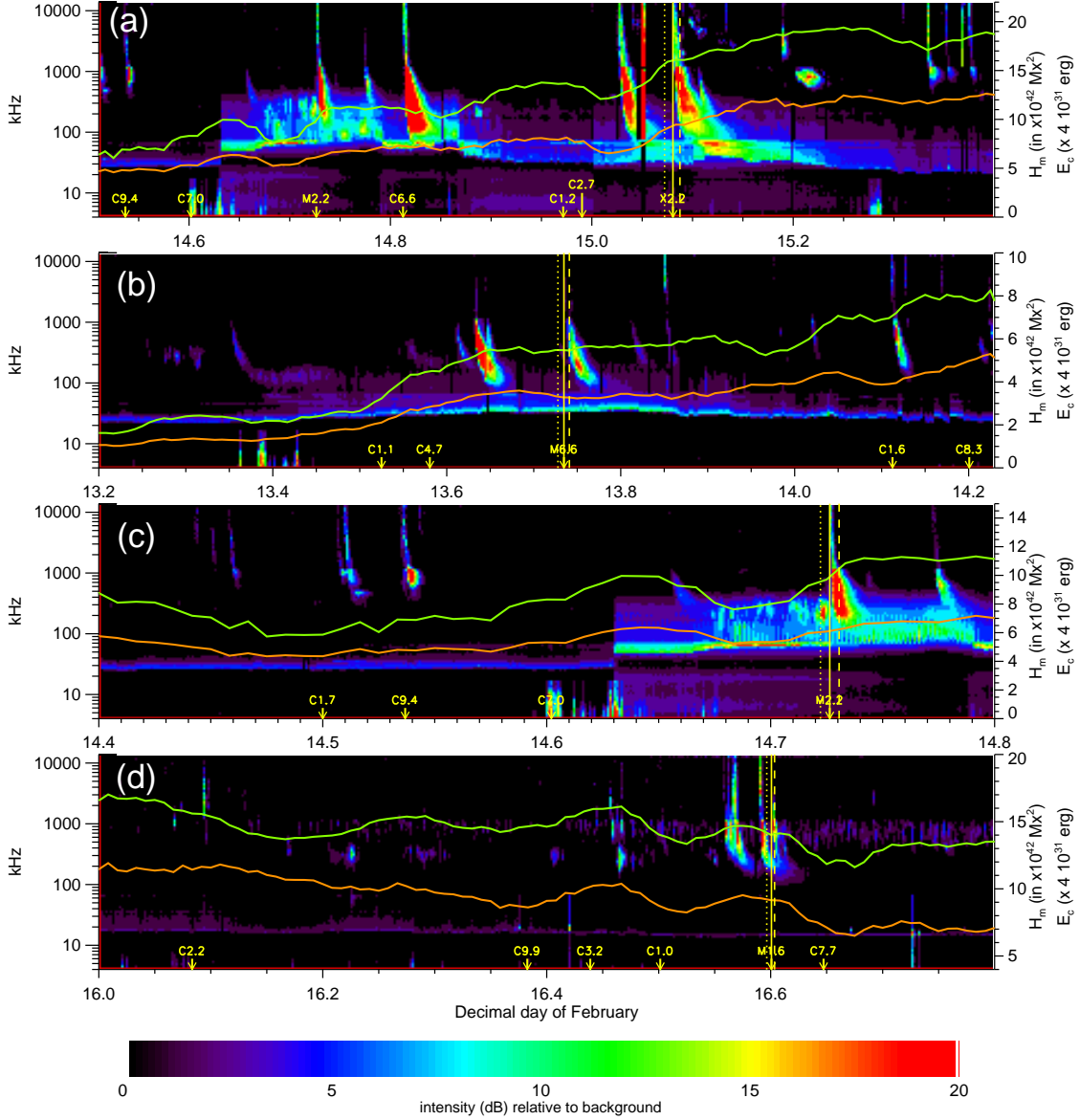


Fig. 11.— 72-minute averages of the relative magnetic helicity H_m (green curves) and free magnetic energy E_c (orange curves) around the times of the four largest eruptive flares triggered in NOAA AR 11158. These flares are the (a) X2.2 flare 15-Feb-2011, (b) M6.6 flare of 13-Feb-2011, (c) M2.2 flare of 14-Feb-2011, and (d) M1.6 flare of 16-Feb-2011. Onset times, peaks, and end times of these flares as registered by GOES are shown by dotted, solid, and dashed lines, respectively. Peak times of additional flares triggered in the AR are also indicated. Overplotted for reference are co-temporal *Wind*/WAVES frequency–time radio spectra.

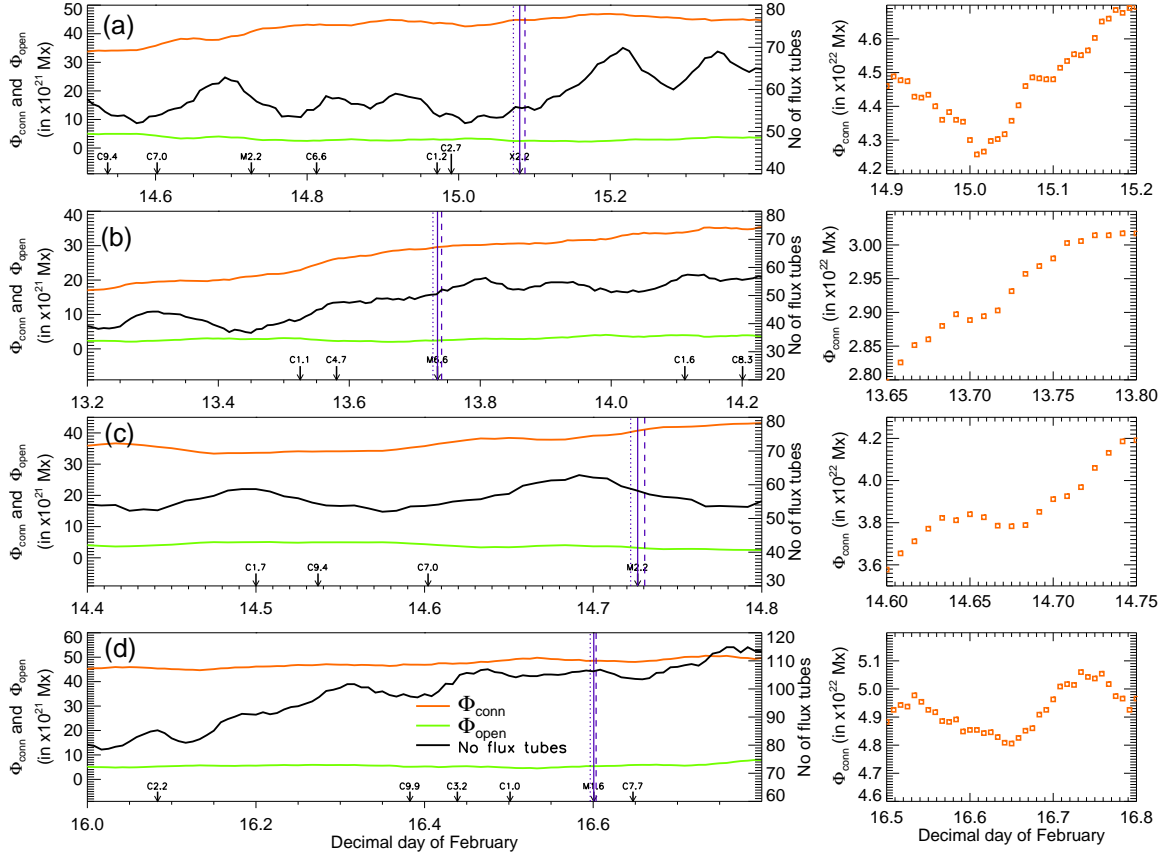


Fig. 12.— Same as Figure 11 but showing the 72-minute-averaged timeseries of the total connected flux Φ_{conn} (orange curves), the total open flux Φ_{open} (green curves), and the number of flux tubes participating in the connectivity matrix of NOAA AR 11158. For each plot, the timeseries of the connected flux Φ_{conn} at the time of the decrease are shown in the insets at the right.